Materials Advances

ROYAL SOCIETY OF CHEMISTRY

PAPER

View Article Online
View Journal | View Issue

Cite this: *Mater. Adv.*, 2024, **5**, 8238

Multifunctional NaEu(WO$_4$)$_2$: defect-tuned red emission and acetone sensing at room temperature†

Kumar Riddhiman Sahoo,[a] Tanushri Das,[b] Mrinal Pal,[b] Mohammad Rezaul Karim,[c] Asiful H. Seikh[c] and Chandan Kumar Ghosh *[a]

Rare-earth double tungstate NaEu(WO$_4$)$_2$ was synthesized *via* a trisodium citrate (Na$_3$cit)-assisted hydrothermal technique, followed by calcination, to promote crystallinity and detailed investigations on their crystal structures and luminescence properties. In this study, the structural evolution of our samples synthesized with different amounts of Na$_3$cit was studied by employing X-ray diffraction, Rietveld refinement, Fourier transform infrared and Raman spectroscopy techniques. It was found that NaEu(WO$_4$)$_2$ belongs to the scheelite family with Na and Eu atoms occupying the same sites and $\mathrm{Eu}_{\mathrm{Na}}^{m\bullet}$ antisite defects deforming EuO$_8$ dodecahedra. The modulation of W–O, Eu–O and angle splitting in the presence of $\mathrm{Eu}_{\mathrm{Na}}^{m\bullet}$ antisite defects was identified. From in-depth X-ray photoelectron spectroscopy, we validated the deformation of the EuO$_8$ dodecahedron due to the presence of oxygen vacancies (V$_\mathrm{O}$s), which originated from $\mathrm{Eu}_{\mathrm{Na}}^{m\bullet}$ antisite defects. Herein, we show that the band gap of NaEu(WO$_4$)$_2$ is highly sensitive to defects; however, the $^5D_0$–$^7F_2$ transition of Eu^{3+} at 615 nm with color coordinates (0.67, 0.33) is very robust, making NaEu(WO$_4$)$_2$ a suitable red phosphor material for near UV-type light-emitting devices (LEDs). We also identified that V$_\mathrm{O}$s present in the EuO$_8$ dodecahedron act as active sites for acetone sensing (~68% response to 100 ppm) with a response and recovery time of ~3.3/10 s at room temperature, suggesting the potency of NaEu(WO$_4$)$_2$ as a multifunctional material with applications in LEDs and acetone sensors. In order to validate our experimental observations theoretically, we calculated the band structure and density of states of bare and $\mathrm{Eu}_{\mathrm{Na}}^{m\bullet}$ antisite defects containing NaEu(WO$_4$)$_2$ using *ab initio* density functional theory and identified the sensing mechanism. We believe that our studies will be helpful in introducing new multifunctional applications of NaEu(WO$_4$)$_2$, while theoretical calculations will provide new electronic insights that may be used to understand the features of other double rare-earth tungstate materials.

Received 15th June 2024,
Accepted 15th September 2024

DOI: 10.1039/d4ma00617h

rsc.li/materials-advances

1. Introduction

Motivated by multifunctional materials in nature such as the human skin and bird feathers, the design and development of materials having multiple functionalities has become an upcoming field for various sustainable applications and has gained the attention of researchers in the recent past. Owing to their multiple features, scheelite-type alkali rare-earth double tungstates (A$^\mathrm{I}$Ln(WO$_4$)$_2$, A = alkali metal, Ln = lanthanide rare-earth metal) with C_{4h} symmetry and the $I4_1/a$ space group have emerged as promising materials in many technologically diverse areas such as catalysis, energy storage, scintillators, and laser hosts. Because of the strong covalence of the W–O bond, scheelites act as good hosts that promote high solubility for lanthanide (Ln) doping, where they exhibit narrow emission characteristics of high spectral purity due to the strong f–f or f–d transition of Ln^{3+} ions.[1] It is worth mentioning that the absorption coefficient of Ln^{3+} ions is usually very low, resulting in a weak emission signal.[2] However, tungstates, because of their strong absorption coefficient, facilitate energy transfer to Ln^{3+}, and subsequently, the emission intensity gets enhanced.[3] Because of this, Ln^{3+}-doped tungstate scheelites show maximum performance in the field of solid-state lighting devices, including field emission displays, plasma display panels, liquid crystal displays, and light-emitting diodes (LEDs). These lighting systems have several advantages of biocompatibility, low power consumption, long lifetime, remarkably high brightness, *etc.*, and hence have high market value. As different Ln^{3+} ions

---

[a] *School of Materials Science and Nanotechnology, Jadavpur University, Jadavpur, Kolkata-700032, India. E-mail: chandu_ju@yahoo.co.in; Tel: +91 033-2457-3028*

[b] *CSIR-Central Glass and Ceramic Research Institute, Kolkata-700032, India*

[c] *Center of Excellence for Research in Engineering Materials (CEREM), Deanship of Scientific Research, College of Engineering, King Saud University, Riyadh, 11421, Saudi Arabia*

† Electronic supplementary information (ESI) available. See DOI: **https://doi.org/10.1039/d4ma00617h**

have different energy levels and accordingly produce different colors, the choice of Ln^{3+} is most important to tune the color output of the lighting devices as per requirements and applications.[4] In general, the energy transfer between tungstate and Ln^{3+} ions significantly depends on the type of Ln^{3+} and host matrix, wherein efforts are mostly given to explore different tungstate hosts for improved energy transfer. In contrast to Ln^{3+}-doped tungstates, self-contained tungstate–lanthanide hosts have been found to be highly efficient for this process, wherein scheelite-structured alkali metals, *i.e.*, Ln-binary tungstate with the generic formula $\mathrm{A^ILn(WO_4)_2}$, a representative of new scheelite materials with high density and low phonon threshold,[5] have drawn worldwide attention. Much more improved emission has been detected from $\mathrm{A^ILn(WO_4)_2}$, suggesting their suitability for several lighting systems including laser crystals and phosphors.[6] It has been found that 'A' is commonly responsible for crystal field distortion around Ln^{3+} ions, relaxing the selection rules for f–f or f–d transitions, which enhance emission intensity.[7] Among several Ln^{3+} ions such as Gd^{3+}, Lu^{3+}, Tm^{3+}, and Dy^{3+}, several works have been carried out with Eu^{3+}-doped binary tungstate as the designing red phosphor due to its high absorption coefficient in UV/near UV region, which circumvents low color rendering index in comparison with other Eu^{3+}-doped metal oxides/sulphides (*e.g.*, ZnO, $\mathrm{SnO_2}$, and ZnS) and scheelites (*e.g.*, $\mathrm{SrWO_4}$).[8–11] Nevertheless, there is still a need to improve the Eu^{3+}-red phosphor, wherein researchers are actively involved. In this regard, it may be stated that few fundamental studies are likely to explore the structure and optical emissions from $\mathrm{NaEu(WO_4)_2}$, indicating its potency as a red phosphor material. As an example, J. Huang *et al.* have investigated the effect of alkali metal ions on the local structure of $\mathrm{AEu(WO_4)_2}$ (A = Li, Na, K), where they identified broader red emission at 614 nm due to an effective charge transfer excitation in $\mathrm{KEu(WO_4)_2}$ in comparison with that of $\mathrm{LiEu(WO_4)_2}$ and $\mathrm{NaEu(WO_4)_2}$.[12] Neeraj *et al.* observed a significant improvement in the light output in $\mathrm{NaY_{0.5}Eu_{0.5}(WO_4)(MoO_4)}$ with reference to the commercial red phosphor $\mathrm{Y_2O_3S{:}Eu^{3+}}$.[13] Commonly, the $\mathrm{A^ILn(WO_4)_2}$ class of materials is synthesised by several techniques such as solid state reaction, hydrothermal, solvothermal, and microwave synthesis.[14] Several researchers, including our group, have found that defects depending on the synthesis protocols play an important role in tuning the distortion around Ln^{3+} ions and accordingly, the selection rules get relaxed. Therefore, it may be stated that emission is significantly dependent on the synthesis methods, where some studies are going on actively.[15] As an example, the use of water and ethylene glycol during the solvothermal synthesis of $\mathrm{NaEu(WO_4)_2}$ significantly alters the Eu–O bond lengths, which in consequence could cause a blue shift of the charge transfer band,[16] while Munirathnappa *et al.* tuned the defects by electron beam radiation and observed a significant improvement of the luminescence property of $\mathrm{NaEu(WO_4)_2}$.[17] A careful literature review reveals that few efforts were undertaken to generate various micro/nanostructures of $\mathrm{NaEu(WO_4)_2}$ using different surfactants such as ethylenediaminetetraacetic acid (EDTA), cetyltrimethyl ammonium bromide (CTAB), trisodium citrate ($\mathrm{Na_3cit}$), polyvinylpyrrolidone (PVP), and ethylene glycol (EG) and the morphological influences on the emission characteristics were studied. However, there is no report to illustrate the effect of surfactant on the defects, particularly on the distortion of the crystal field around Eu^{3+} ions and related emissions.

Based on our previous investigations[18] and motivated by the fact that defects can be tuned by varying the surfactant during the hydrothermal process, an attempt has been made for the first time to examine the influence of $\mathrm{Na_3cit}$ on the defects and related deformation around the Eu^{3+} ions within $\mathrm{NaEu(WO_4)_2}$. In this study, we have identified that $\mathrm{Na_3cit}$ plays a significant role to tune the $\mathrm{Eu}_{\mathrm{Na}}^{m\bullet}$ antisite defects, which are subsequently counterbalanced by the oxygen vacancy ($\mathrm{V_O}$). We have also emphasized the $\mathrm{V_O}$-induced modification of the bond length and mixing of Eu 4f orbitals, which synergistically impact the emission properties and chromaticity coordinates. Most importantly, by varying the synthesis condition, we achieved the chromaticity coordinate (0.667, 0.333) from one of our synthesized samples, which perfectly matches with that of the National Television Standard Committee (NTSC)-prescribed chromaticity coordinate for red phosphor.

In the recent past, there has been an increasing interest in the detection of life-threatening toxic gases. Although techniques like as gas/liquid chromatography exist, because of their high cost, their wide application is limited. Herein, chemo-resistive-type gas sensors based on metal oxides have been viewed as one of the most economical, effective, and fast techniques for sensing applications. However, major issues still exist in their high sensitivity and high temperature (∼250–400 °C) operation.[19] Hence, it is worthwhile to develop a room temperature sensor with low power consumption, safety, and long lifetime. Though sensors operating at higher temperature are largely reported, room temperature sensors are very rare. However, efforts are continuously underway to find out suitable materials for room-temperature sensors. Our previous investigations reveal that $\mathrm{V_O}$ often leads to the gas sensing property;[15,18] hence, we checked the gas sensing property of $\mathrm{NaEu(WO_4)_2}$ and, most importantly, acetone sensing has been achieved at room temperature. Apart from the experimental investigations on the optical and gas sensing properties, *ab initio* density functional theory has been adopted to acquired knowledge of the band structure and partial density of states (PDOS) of $\mathrm{NaEu(WO_4)_2}$ in order to understand $\mathrm{Eu}_{\mathrm{Na}}^{m\bullet}$ antisite defect-induced changes in the optical and acetone sensing properties of $\mathrm{NaEu(WO_4)_2}$. To the best of our knowledge, no such study exists for $\mathrm{NaEu(WO_4)_2}$; hence, we believe that these experimental and theoretical findings will be helpful in realizing the multifunctional applications of $\mathrm{NaEu(WO_4)_2}$.

2. Experimental section

2.1. Synthesis of $\mathrm{NaEu(WO_4)_2}$

Sodium europium double tungstate ($\mathrm{NaEu(WO_4)_2}$) was synthesized by a facile hydrothermal method. Initially, 1.00 mmol (0.338 g) of europium nitrate hydrate [$\mathrm{Eu(NO_3)_3{\cdot}H_2O}$, Alfa Aesar] and tri-sodium citrate dihydrate [$\mathrm{Na_3cit}$, Merck] were dissolved in 50.00 mL DI solution and stirred for 20 minutes. Another 20.00 mL aqueous solution containing 2.00 mmol (0.660 g) sodium tungstate dihydrate [$Na_2WO_4{\cdot}2H_2O$, Sigma Aldrich] was added dropwise to the previously prepared solution and stirred (30 minutes) for homogeneous mixing. Then, the mixture solution was transferred to a Teflon-lined stainless-steel autoclave of 100.00 mL capacity for hydrothermal reaction, which was carried out at 180 °C for 24 h. After the reaction, the temperature was cooled down and the powder sample was collected by means of centrifugation at 12 000 rpm, followed by washing with DI water and ethanol twice and drying at 70 °C for 24 h. The obtained powder was calcined at 800 °C under nitrogen (N_2) atmosphere for 5 h and the final product was obtained. In order to examine the effect of Na_3cit on the final product, we varied the Na_3cit (*ca.* 0.75, 0.50 and 0.25 mmol) amount during the hydrothermal reaction, keeping all other parameters same. Accordingly, they were named as $NEWO_{0.75}$, $NEWO_{0.50}$ and $NEWO_{0.25}$, respectively.

2.2. Characterization techniques

Structural analysis and phase confirmation were using the X-ray diffraction (XRD) patterns collected on a Rigaku (Japan) Ultima III powder diffractometer equipped with a Cu Kα radiation source (λ = 1.5406 Å). The Rietveld refinement was done with the help of FullProf Suite software to determine the structural and microstructural parameters. The background was fitted with linear interpolation, while the Pseudo-Voigt profile with asymmetry was used for the peak shape. The morphology was examined by field emission scanning electron microscopy (FESEM, S-4800, Hitachi Japan). Vibrational analysis was done using Fourier transform infrared spectroscopy (Shimadzu, IRPrestige-21) and Raman spectroscopy (alpha 300 Witec, 530 nm laser, 3 mW power and 2 m spot size). Elemental analysis was performed using X-ray photoelectron spectroscopy (PHI 5000 Versa Prob II, FEI Inc., Al Kα radiation, 1486 eV). The optical properties were investigated by a UV-vis (V-630, JASCO) and a photoluminescence spectrophotometer (RF-5301, Shimadzu). The measurement of luminescence lifetime was carried out with the help of the time-correlated single photon counting set up by Horiba Jobin-Yvon. The luminescence decay time was collected through a Hamamatsu MCP photomultiplier (R3809) and analysed using IBH DAS6 software.

2.3. Measurement of the gas-sensing properties of $NaEu(WO_4)_2$

Taguchi-type sensor modules were fabricated with a cylindrical alumina substrate wherein Pt wires and conducting gold paste were used for electroplating the alumina substrates. By mixing the as-synthesised materials with isopropyl alcohol, a slurry paste of desired consistency was prepared and the paste was drop-coated on the substrate and dried for 6 h to get rid of residue solvents. Ni–Cr wire, used as heating coils, was inserted inside the hollow of the alumina substrate. Then, the sensor modules, prepared by wielding the substrates on a six-pin socket, were used to evaluate the gas sensing properties in the presence of different volatile organic compounds (VOCs), namely, ammonia, acetone, ethanol, formalin, methanol, and isopropyl alcohol. The response was evaluated using the formulae $S\,(\%\ \text{response}) = \dfrac{R_{\text{gas}} - R_{\text{air}}}{R_{\text{air}}} \times 100$, where R_{gas} and R_{air} denote the resistance of the sensor in the absence and presence of the target gas, respectively. The response and recovery time of the sensors were determined from the time taken by the sensor to reach the 90% resistance change with respect to the equilibrium state resistance after exposing and removing the target gas.

2.4. *Ab initio* calculation using density functional theory

The first principles density functional theory (DFT) calculation was carried out in the plane wave pseudo-potential basis, as implemented in the Vienna *ab initio* simulation package the (VASP) using generalized gradient approximation (GGA) exchange–correlation potential. The cutoff energy of the plane wave basis was set to 500 eV, which was sufficient to achieve convergence, while 5 × 5 × 2 Monkhorst–Pack mesh was used for Brillouin zone sampling. The applied Hellmann–Feynman forces on each atom and EDIFF parameter were fixed to 0.015 eV $Å^{-1}$ and 10^{-6} eV for these calculations.

Furthermore, the adsorption energy of acetone on the slab surface was calculated to overcome the antisite defect-induced gas sensing operation. Herein, we considered a vacuum region of 15 Å to avoid interlayer interactions along the *z*-axis, while the 5 × 5 × 1 Monkhorst–Pack mesh and 500 eV cut off energy were employed to get converged free energy for the surface calculation. To understand the adsorption mechanism, isolated acetone molecules were modelled above the cleaved (0 0 4) surface (most stable surface with minimum free energy), keeping acetone at the centre of the unit cell using three configurations (*i.e.*, vertical, parallel to the *x*-axis and parallel to the *y*-axis). The adsorption was determined from eqn (1)[20]

$$E_{\text{ads}} = E_{\text{slab+gas}} - (E_{\text{slab}} + E_{\text{gas}}) \tag{1}$$

where, $E_{\text{slab+gas}}$, E_{slab} and E_{gas} represent the total energy of the slab including gas, total energy of the slab and energy of the isolated gas, *i.e.*, acetone. Within this definition, a negative binding energy is attributed to an exothermic process.

3. Results and discussion

3.1. Phase, crystal structure and micro-structural analyses of $NaEu(WO_4)_2$ by XRD and FESEM

The XRD patterns of all the samples (as shown in Fig. S1, ESI†) consist of strong, sharp diffraction peaks matched closely with tetragonal $NaEu(WO_4)_2$ (JCPDS no. 04-002-3849, space group $I4_1/a$).[12] The absence of any deleterious secondary peak in the diffraction patterns is imperative to point out the formation of the pure phase of the samples. Meanwhile, a crystallite size of ∼33–43 nm was obtained from the well-known Scherer's relation for all the samples, while the strain (ε), calculated using the relation $\varepsilon = \dfrac{\beta}{4\tan(\theta)}$, where β and θ denote the full width at half maxima (FWHM) and Bragg's angle respectively, was calculated to be $\sim 3.40 \times 10^{-3}$, 3.14×10^{-3}, and 2.59×10^{-3} for $NEWO_{0.75}$,

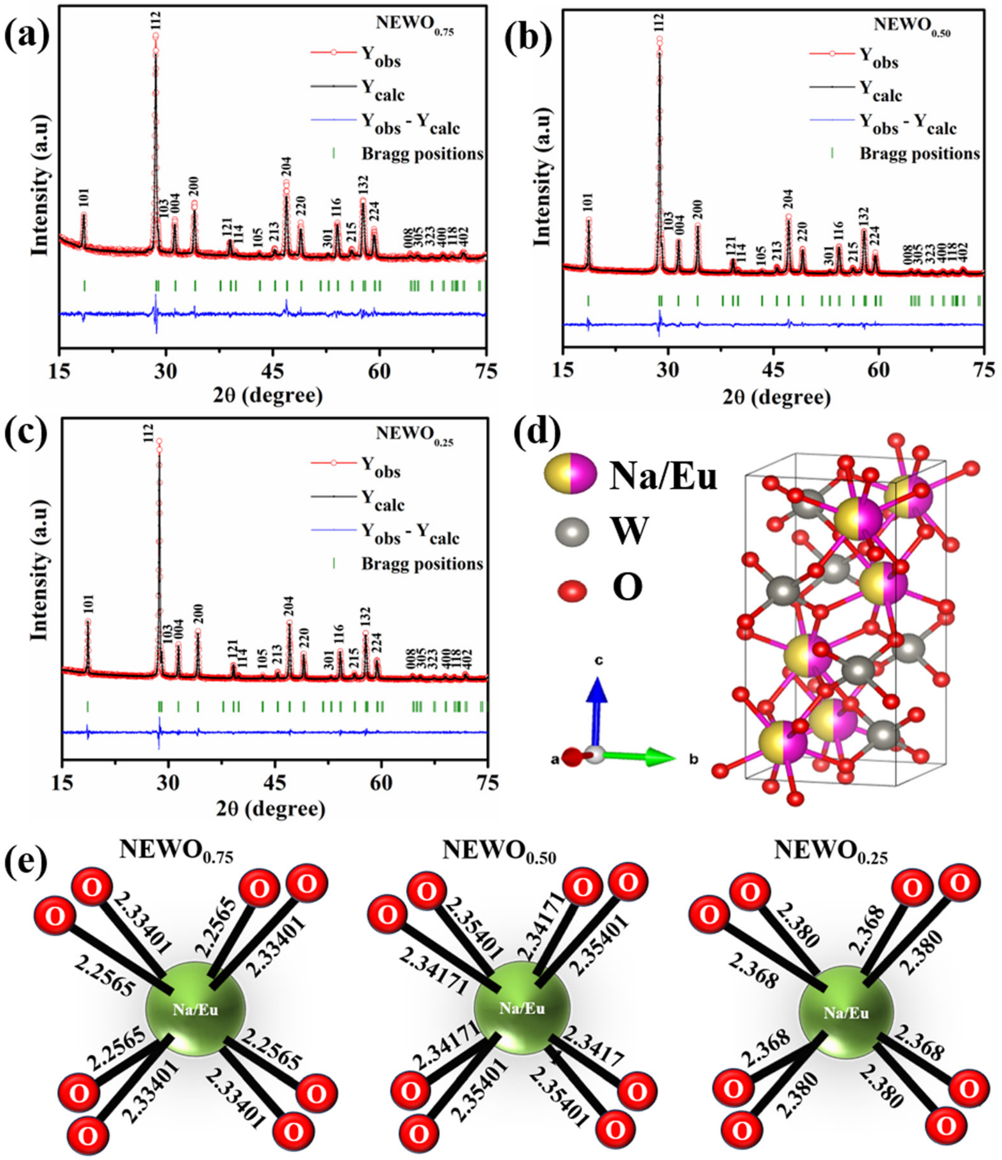

Fig. 1 The observed and refined XRD pattern of $NaEu(WO_4)_2$ samples: (a) $NEWO_{0.75}$, (b) $NEWO_{0.50}$, (c) $NEWO_{0.25}$, (d) unit cell of the $NaEu(WO_4)_2$ tetragonal structure and (e) the schematic representation of the variation in the bond lengths of the Na/Eu–O dodecahedron in $NaEu(WO_4)_2$.

$NEWO_{0.50}$, and $NEWO_{0.25}$, respectively. It is noteworthy that Na_3cit does not have a significant effect on the particle size during the hydrothermal reaction; rather, it has significant impact on 'ε', which may be related to the structural distortion.

Rietveld refinement (shown in Fig. 1(a)–(c)), adopted to study long-range structural order–disorder, provides lattice parameters, unit cell volumes, and lengths of the links between (W–O)/(Na/Eu–O) of all the samples, as summarized in Table 1. Note that these parameters are very close to the data published in the literature[12,16] as well as goodness-of-fit (*e.g.*, χ^2), which indicates the reliability of the refinement process. The unit cell of $NaEu(WO_4)_2$, modelled using the refined parameters for the visualization in the electronic and structural analysis (VESTA) program, consists of the $[WO_4]$ tetrahedron with T_d symmetry group and the $(Na/Eu)O_8$ dodecahedron, where Na^+ and Eu^{3+} are randomly distributed over the same site positions with S_4 symmetry (without an inversion symmetry) (as shown in Fig. 1(d)) and corresponds to two different Eu–O bond lengths (shorter and longer), denoted by $[Eu–O]_s$ and $[Eu–O]_l$, respectively, indicating the distortion of the $(Na/Eu)O_8$ dodecahedron.[21] This distortion (*e.g.*, $\Delta_{Na/Eu-O}$), estimated from $\Delta_{Na/Eu-O} = \frac{1}{8}\sum_{i=1}^{8}\frac{\left|d^{i}_{Na/Eu-O} - \langle d_{Na/Eu-O}\rangle\right|}{\langle d_{Na/Eu-O}\rangle}$, where $\langle d_{Na/Eu-O}\rangle$ denotes average Na/Eu–O bond length, (schematically shown in Fig. 1(e) for all the samples), decreases monotonically from $NEWO_{0.75}$ to $NEWO_{0.25}$.[21] The peculiarity of the hydrothermal method, where varying the Na_3cit concentration commonly influences the organization of the $[(Na/Eu)O_8]$ dodecahedron, which causes various structural defects in the form of V_O, distortion of the bonds, stresses, and strain on the crystallite lattices. Presently $\Delta_{Na/Eu-O}$, ascribed to 'ε', is believed to be

Table 1 Refined parameters from the Rietveld refinement method using FullProf suite software

Parameters		NEWO$_{0.75}$	NEWO$_{0.50}$	NEWO$_{0.25}$
Lattice parameters	$a = b$ (Å)	5.2586 (2)	5.24393 (8)	5.25153 (6)
	c (Å)	11.4182 (6)	11.3766 (3)	11.3979 (2)
Unit cell volume	V (Å^{-3})	315.74 (2)	312.843 (14)	314.3378 (8)
Bond length (in Å)	Na/Eu–O	2.2565 (8)	2.34171 (5)	2.368 (9)
		2.33401 (9)	2.35401 (4)	2.380 (9)
	W–O	2.05794 (7)	1.94063 (3)	1.914 (8)
Bond distance distortion index ($\Delta_{\text{Na/Eu–O}}$)		16.88	2.62	2.53
R_p (%)		5.10	4.63	4.74
R_{wp} (%)		6.60	6.11	6.17
R_{exp} (%)		5.75	4.90	5.59
χ^2		1.32	1.56	1.22

dependent on V$_O$, which can be explained as follows: we have noticed an enhancement in the (Na/Eu)–O bond length and reverse trend for W–O, which, according to Li *et al.*, can be attributed to the decreasing dipole–dipole interactions due to charge entrapment at the V$_O$ site, which gets formed due to the $\text{Eu}_{\text{Na}}^{m\bullet}$ antisite defect at the 4a site, as given by $0 \rightarrow \text{Eu}_{\text{Na}}^{m\bullet} + \text{V}_{\text{O}}^{n\bullet}$.[22,23] Hence, the gradual decrease of $\Delta_{\text{Na/Eu–O}}$ from NEWO$_{0.75}$ to NEWO$_{0.25}$ may be ascribed to the reduced $\text{Eu}_{\text{Na}}^{m\bullet}$ antisite defect. In our case, the hydrothermal reaction of Na$^+$, Eu^{3+}, and WO$_4{}^{2-}$ ions resulted in the formation of NaEu(WO$_4$)$_2$ precipitates, which can be shown in eqn (2)–(6) below.[24–26]

$$\text{Na}_2\text{WO}_{4(\text{aq})} \rightarrow 2\text{Na}^+{}_{(\text{aq})} + (\text{WO}_4)^{2-}{}_{(\text{aq})} \tag{2}$$

$$\text{Eu(NO}_3)_{3(\text{aq})} \rightarrow \text{Eu}^{3+}{}_{(\text{aq})} + 3\text{NO}^-{}_{(\text{aq})} \tag{3}$$

$$\text{Na}_3\text{cit}_{(\text{aq})} \rightarrow 3\text{Na}^+{}_{(\text{aq})} + \text{cit}^{3-}{}_{(\text{aq})} \tag{4}$$

$$\text{Eu}^{3+}{}_{(\text{aq})} + \text{cit}^{3-}{}_{(\text{aq})} \rightarrow [\text{Eu}^{3+}\text{–cit}^{3-}]\ \text{complex}_{(\text{aq})} + \text{NaNO}_{3(\text{aq})} \tag{5}$$

$$2[\text{Eu}^{3+}\text{–cit}^{3-}]\ \text{complex}_{(\text{aq})} + 2\text{Na}^+{}_{(\text{aq})} + 2(\text{WO}_4)^{2-}{}_{(\text{aq})} \rightarrow 2\ \text{NaEu(WO}_4)_{2(\text{S})} + 2\text{cit}^{3-}{}_{(\text{aq})} \tag{6}$$

The [Eu^{3+}–cit^{3-}] complex plays a pivotal role in the synthesis of NaEu(WO$_4$)$_2$, specifically on $\text{Eu}_{\text{Na}}^{m\bullet}$. Low Na$_3$cit concentration inhibits the formation of the [Eu^{3+}–cit^{3-}] complex, which as a result reduces the $\text{Eu}_{\text{Na}}^{m\bullet}$ antisite defect. According to Shannon's data, the ionic radius of Na$^+$ (1.18 Å) is larger than that of Eu^{3+} (0.947 Å); therefore, the equivalent radius of A-site $r_A = \frac{1.18 + 0.947}{2} + x\text{Eu}_{\text{Na}}^{m\bullet}$ Å,[27] where 'x' represents the fraction of the antisite defect, suggesting that a decrease of the $\text{Eu}_{\text{Na}}^{m\bullet}$ antisite defect will increase the (Na/Eu)–O bond length, in good agreement with our experimental findings. The FESEM images of the samples shown in Fig. 2(a)–(c) illustrates the agglomerated nature of the particle, which may be attributed to the calcination effect at 800 °C.

3.2. Investigations of the defects in NaEu(WO$_4$)$_2$ by FTIR, Raman and X-ray photoelectron spectroscopy techniques

In order to judge the structural distortion of the dodecahedron due to the $\text{Eu}_{\text{Na}}^{m\bullet}$ antisite defect, the FTIR and Raman spectra were taken as these spectroscopic techniques invaluably illustrate the short-range order–disorder phenomenon.[28] The FTIR spectra (Fig. S2, ESI†), measured in the range of 400–1000 cm^{-1}, consists of four absorption bands at 412–418, 438–440, 714–725 and 775–852 cm^{-1} indexed to internal O–W–O symmetric stretching, O–W–O symmetric bending, O–W–O anti-symmetric stretching (1E$_u$), and O–W–O anti-symmetric stretching (1A$_u$) vibrations, respectively,[28,29] while the band at 515–555 cm^{-1} is attributed to the Eu–O stretching vibration.[30,31] Deconvolution reveals two distinct peaks (shown in the inset of Fig. 3(a)–(c)) measured at 524.5 and 548.1 cm^{-1} for NEWO$_{0.75}$, 524.3 and 547.2 cm^{-1} for NEWO$_{0.50}$, and 521.9 and 542.3 cm^{-1} for NEWO$_{0.25}$. Herein, we believe that these two peaks originate from the deformed EuO$_8$ dodecahedra containing the $\text{Eu}_{\text{Na}}^{m\bullet}$ antisite defect, *i.e.*, [EuO$_8$]$_{\text{deformed}}$ and EuO$_8$ dodecahedra without the antisite defect, *i.e.*, [EuO$_8$]$_{\text{ordered}}$.[32] [EuO$_8$]$_{\text{deformed}}$ was estimated from the FTIR spectra using the relation $\frac{|A_{\text{deformed}} - A_{\text{ordered}}|}{A_{\text{deformed}} + A_{\text{ordered}}}$, where A_{deformed} and A_{ordered} denote the area under the curves corresponding to [EuO$_8$]$_{\text{deformed}}$ and [EuO$_8$]$_{\text{ordered}}$, showing a decreasing trend (~0.80, 0.51 and 0.19 for NEWO$_{0.75}$, NEWO$_{0.50}$ and NEWO$_{0.25}$,

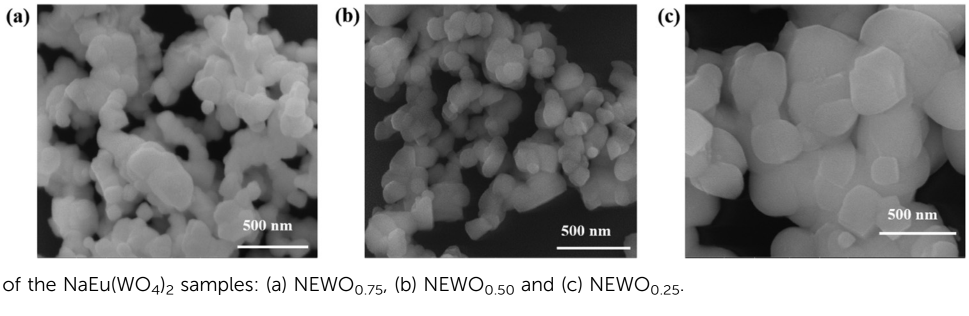

Fig. 2 FESEM image of the NaEu(WO$_4$)$_2$ samples: (a) NEWO$_{0.75}$, (b) NEWO$_{0.50}$ and (c) NEWO$_{0.25}$.

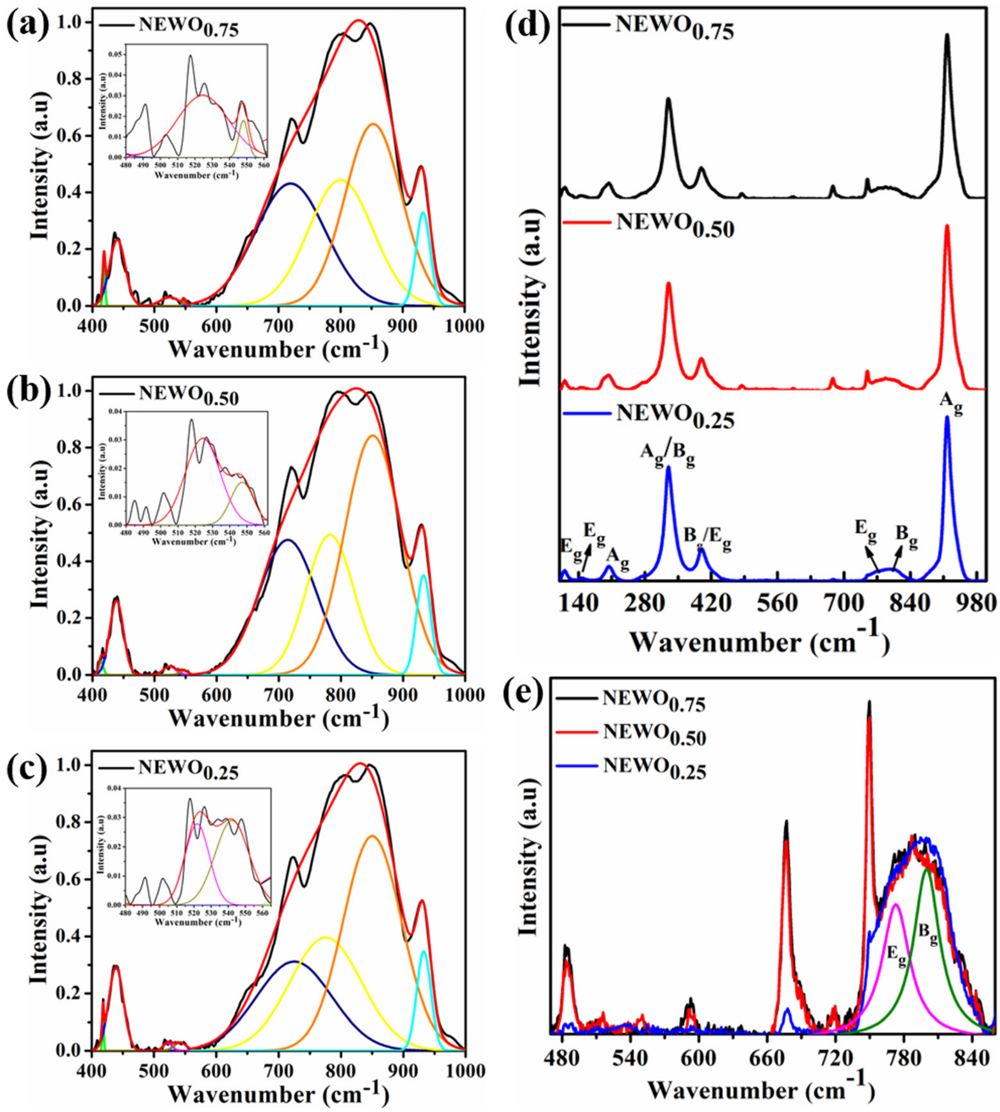

Fig. 3 Deconvoluted peaks of the FTIR spectrum: (a) NEWO$_{0.75}$, (b) NEWO$_{0.50}$, and (c) NEWO$_{0.25}$. (d) Raman spectra of NEWO$_{0.75}$, and NEWO$_{0.50}$, NEWO$_{0.25}$. (e) Magnified Raman spectra (480–840 cm^{-1}).

respectively), which is in good agreement with the Rietveld results of the decreasing $\mathrm{Eu}_{\mathrm{Na}}^{m\bullet}$ antisite defect.

According to group theory calculation, only thirteen Raman vibrational modes of tetragonal scheelite materials at the Γ-point are active and represented by eqn (7)[28]

$$\Gamma = 3A_g + 5B_g + 5E_g \quad (7)$$

where non-degenerate A$_g$, B$_g$ modes and doubly degenerate E$_g$ mode originate from various internal vibrations of $[WO_4]^{2-}$ with the S_4 point symmetry or external vibrations of the (Na/Eu)O$_8$ dodecahedron with D_{2d} point symmetry. Herein, Raman spectrum of all sample (Fig. 3(d)), measured in between 100–1000 cm^{-1}, comprises of eight peaks, measured at 111, 147, 203, 329, 399, 763, 800 and 917 cm^{-1}, while NEWO$_{0.50}$ and NEWO$_{0.75}$ show three additional peaks. Very briefly, the peak at 111 cm^{-1} is assigned to the E$_g$ stretching vibration of the (Na/Eu)O$_8$ dodecahedron or the translational mode of Na$^+$ and Eu^{3+},[33] while the peaks at 147 and 203 cm^{-1} are indexed to the E$_g$ and A$_g$ free rotation of $[WO_4]^{2-}$, respectively.[34] The peaks at 329 and 399 cm^{-1} are ascribed to the A$_g$ anti-symmetric and B$_g$ symmetric bending of O–W–O,[35] while the peaks at 763 and 800 cm^{-1} are ascertained to the B$_g$ and E$_g$ anti-symmetric stretching of the O–W–O vibrations, respectively.[36] The peak at 918 cm^{-1} is attributed to the A$_g$ symmetric O–W–O stretching.[37] In contrast to NEWO$_{0.25}$, three additional peaks of comparatively low intensity (zoomed-in image shown in Fig. 3(e)) have been identified at 484, 677 and 750 cm^{-1} for NEWO$_{0.50}$ and NEWO$_{0.75}$, and they can be readily ascribed to $[(Na/Eu)O_8]_{deformed}$ of NEWO$_{0.50}$ and NEWO$_{0.75}$, thus validating previous studies.[38]

To accumulate more information about the chemical bonding characteristics of the constituent elements in the presence of $[(Na/Eu)O_8]_{deformed}$, we adopted XPS to examine the valence state of Na, Eu, W and O. Herein, all the measured binding energy data have been corrected with reference to C 1s with a binding energy at 284.6 eV, which appears as an environmental carbon. The XPS survey spectra (Fig. S3, ESI†), recorded in between 0 and 1100 eV, represents a core binding energy of Na, Eu, W and O of $NEWO_{0.75}$, $NEWO_{0.50}$, and $NEWO_{0.25}$, while the high-resolution spectra of Eu and O, W and Na were also recorded. As illustrated in Fig. 4(a), (c) and (e), the high-resolution Eu spectrum consists of two peaks at 135.9 and 141.8 eV corresponding to the spin–orbit splitting of $4d_{5/2}$ and $4d_{3/2}$ orbitals, respectively, in accordance with its trivalent oxidation state.[39] As these spectra are asymmetric, hence, a careful deconvolution demonstrates two peaks (denoted by E_a and E_b) for $4d_{5/2}$ orbitals with a binding energy of 135.0, 136.8 eV for $NEWO_{0.75}$, 135.2, 137.0 eV for $NEWO_{0.5}$ and 136.0, 137.5 eV for $NEWO_{0.25}$. Similarly, the binding energies of $4d_{3/2}$ orbitals, after deconvolution (*e.g.*, peak E_c and E_d), were obtained at 140.4, 142.2 eV and 141.0, 142.5 and 141.5, 143.1 eV for the three respective samples. Herein, $4d_{5/2}$ with lower binding energy (*e.g.*, 135.0, 135.2 and 136.0 eV for $NEWO_{0.75}$, $NEWO_{0.5}$ and $NEWO_{0.25}$ respectively) is assigned to $[EuO_8]_{ordered}$, while a higher binding energy (*e.g.*, 136.8, 137.0, and 137.5 eV for $NEWO_{0.75}$, $NEWO_{0.5}$ and $NEWO_{0.25}$, respectively) corresponds to $[EuO_8]_{deformed}$. Two different binding energies denote the presence of Eu^{3+} with two different polarizing fields, which can be normally expressed by $\varphi_{eff} = \dfrac{Z_{eff}}{r}$, where Z_{eff} and '*r*' denote nuclear charge and ionic radius in the respective ligand field, respectively, while φ_{eff} is the effective ionic potential and denotes the polarizability of the Eu^{3+} ion.[40] In brief, due to the less difference between the electronegativity of O (3.44) and Eu (1.2), the Eu–O bond is covalent, where electrons are shared by Eu and O. In case of the $[EuO_8]_{ordered}$ dodecahedron, the Eu^{3+} ions are surrounded by eight O atoms, whereas this number is less in the case of $[EuO_8]_{deformed}$ due to the presence of $V_O^{n\bullet}$, suggesting

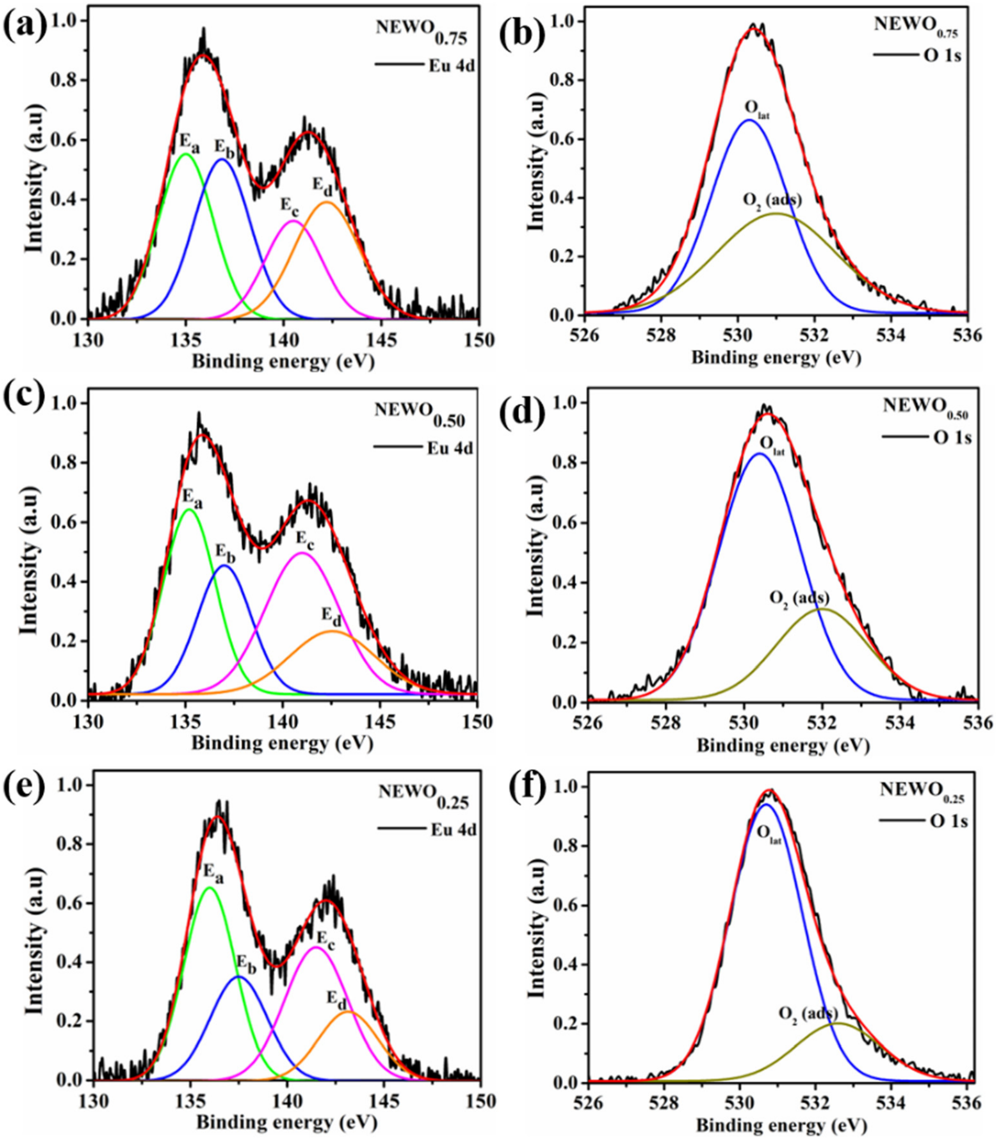

Fig. 4 High-resolution XPS spectra of the Eu 4d state and O 1s state of (a) and (b) $NEWO_{0.75}$. (c) and (d) $NEWO_{0.50}$ and (e) and (f) $NEWO_{0.25}$.

different '*r*' for these two different dodecahedrons; rather, it will be less in $[EuO_8]_{\text{deformed}}$. Therefore, the higher binding energy of Eu 4d orbitals in $[EuO_8]_{\text{deformed}}$ is ascribed to the higher φ_{eff} in the deformed dodecahedron. The $[EuO_8]_{\text{deformed}}$:$[EuO_8]_{\text{ordered}}$ ratio, an indication of the polarizability around Eu^{3+} ions, was estimated from the area under the $4d_{5/2}$ orbital, and this ratio was found to be 1.0, 0.7 and 0.6 for $NEWO_{0.75}$, $NEWO_{0.50}$ and $NEWO_{0.25}$, respectively, indicating a monotonic decrease of $[EuO_8]_{\text{deformed}}$. The covalence of the dodecahedron host, which primarily depends on 'ϕ_{eff}', is believed to be decrease from $NEWO_{0.75}$ to $NEWO_{0.25}$ as the decrease in the $Eu_{Na}^{m\bullet}$ antisite defect makes the dodecahedron more ionic due to the larger electronegativity difference between Na (0.93) and O (3.44). In addition, the increasing binding energy of both $4d_{5/2}$ and $4d_{3/2}$ orbitals from $NEWO_{0.75}$ to $NEWO_{0.25}$ is correlated to the enhancement of the Eu–O bond lengths in good agreement with Rietveld analysis.

For oxygen, the high-resolution O 1s spectra of the three samples are shown in Fig. 4(b), (d) and (f), which is measured at 530.0 eV of the typical asymmetric characteristics, indicating the presence of $V_O^{n\bullet}$ in the samples.[41] After deconvolution, two different bonding states of oxygen with binding energies of 530.3, 531.0 eV for $NEWO_{0.75}$, 530.4, 532.0 eV for $NEWO_{0.50}$ and 530.7, 532.6 eV for $NEWO_{0.25}$ were observed. Low binding energy corresponds to the lattice oxygen (O_{lat}) species of $[EuO_8]_{\text{ordered}}$, while the higher binding energies are attributed to the adsorbed oxygen (O_2(ads)) species at the $V_O^{n\bullet}$ site within $[EuO_8]_{\text{deformed}}$. An increase in the binding energy of O_{lat} is ascribed to the reduced deformation of the $[EuO_8]_{\text{deformed}}$ dodecahedron. However, the O_2(ads)/O_{lat} molar ratio was calculated to be ∼0.44, 0.29 and 0.20 for $NEWO_{0.75}$, $NEWO_{0.50}$ and $NEWO_{0.25}$, respectively; hence, the result indicates a monotonic decrease in $V_O^{n\bullet}$ from $NEWO_{0.75}$ to $NEWO_{0.25}$. As XPS is highly sensitive to the surface, therefore, we believe that these $V_O^{n\bullet}$ mostly resides on the sample surface. In contrast, the spectra of Na and W have been found in the Gaussian shape and were deconvoluted (as shown in Fig. S4, ESI†). From the above FTIR and XPS experiments, we have confirmed that the antisite defect mainly arose due to the Eu elements, which play a key role in the defects.

3.3. Investigation of the optical properties of $NaEu(WO_4)_2$

In order to gain insight into the mechanism on the effect of the $Eu_{Na}^{m\bullet}$ antisite defect on the optical properties, the UV-vis absorption spectra (shown in Fig. S5, ESI†) were recorded and analysed to calculate the band gap (E_g) using Tauc plot.[42] Herein, the direct E_g of NEWO (discussed later) was estimated to be ∼2.24, 2.27 and 2.58 eV for $NEWO_{0.75}$, $NEWO_{0.50}$, and $NEWO_{0.25}$, respectively (shown in Fig. 5(a)–(c)). Such a trend of increasing E_g may be assigned to a decrease in the covalence of the host lattice due to $[EuO_8]_{\text{deformed}}$ and can be explained as follows: mostly, E_g depends on the polarizability of cations and deformation of anions. Greater the cationic polarization and anionic deformation, stronger the covalent links between the anion and cation, thus narrowing the E_g. Our XPS studies reveal that the covalence of the host matrix decreases from $NEWO_{0.75}$ to $NEWO_{0.25}$; thus, the enhancement of E_g can be certainly ascribed to the reduced covalence of the host matrix.

Prior to examining the emission, we recorded the photoluminescence excitation (PLE) spectra of the as-synthesized samples (normalized spectra are shown in Fig. S6(a), ESI†). It is clearly visible that the PLE spectra of all the as-prepared materials consist of three peaks, measured at 380, 392 and 463 nm, which are assigned to $^7F_0$–$^5L_7$, $^7F_0$–$^5L_6$ and $^7F_0$–$^5D_2$ intra-configurational $4f^6$ transitions of Eu^{3+}. One peak, recorded at 360 nm for $NEWO_{0.50}$ and $NEWO_{0.25}$, is ascribed to the $^7F_0$–$^5D_4$ transition of Eu^{3+}, while another peak of relatively low intensity at 413 nm, observed only for $NEWO_{0.25}$, demonstrates the $^7F_0$–$^5D_3$ transition of Eu^{3+}. Careful literature survey reveals that our measured PLE spectra are not very sharp in comparison with other observations and may be ascribed to the distorted dodecahedron.[43] In addition, a sharp peak was also identified at 306 nm, which may be assigned to the charge transfer band (CTB) from the surrounding oxygen anions to the WO_4 tetrahedron. In this context, it may be stated that this is an interesting result for this particular phosphor material because of the fact that they have intense excitation peaks at 380, 392 and 463 nm in the ultra-violet (UV), near-UV, and UV-blue region, respectively, can act as efficient pumping sources for the red emission from Eu^{3+} ions.

Normalized photoluminescence signals under 392 nm excitation wavelength are presented in (Fig. 5(d)). Herein, the spectrum of each sample shows a typical emission band of Eu^{3+} in the range of 555–635 nm, comprising one prominent peak at 615 nm and two relatively less intense peaks at 565 and 592 nm. The peak at 615 nm corresponds to the $^5D_0 \rightarrow {}^7F_2$ electric dipole transition of Eu^{3+}, which is hypersensitive to the local structures of Eu^{3+}, particularly in the non-centrosymmetric crystal site, according to Judd–Ofelt's theory. In contrast, the emission peak at 592 nm, assigned to the $^5D_0 \rightarrow {}^7F_1$ magnetic dipole transition of Eu^{3+}, does not depend on the surrounding environment.[44] It is noteworthy that the ground state electronic configuration of Eu^{3+} has $^7F_0$ non-degenerate and non-overlapping $^{2S+1}L_J$ multiplets; thus, Eu^{3+} is mostly used as an optical probe to investigate the crystal field surrounding them, where the intensity ratio between $^5D_0 \rightarrow {}^7F_2$ and $^5D_0 \rightarrow {}^7F_1$ is used to estimate the asymmetry of the local environment.[45] A very careful estimation reveals that the area under the 615 nm emission curve increases from $NEWO_{0.75}$ to $NEWO_{0.25}$, indicating the reduction of $[EuO_8]_{\text{deformed}}$, in good agreement with the previous XRD and FTIR results. Hence, it may be concluded that the lowering of the Na_3cit concentration reduces the $Eu_{Na}^{m\bullet}$ antisite defect as well as $V_O^{n\bullet}$, which, as a result, increase the symmetry of the crystal structure. The emission peak at 565 nm, attributed to the $^5D_0 \rightarrow {}^7F_0$ transition of Eu^{3+}, has been observed in few other $NaEu(WO_4)_2$-like host matrices including the $LaAlO_3$:Eu^{3+} nanophosphor, $LaPO_4$:Eu^{3+} nanoparticles, SrB_2O_4:Eu^{3+} phosphor, and potassium–aluminoborotellurite.[46–48] In principle, he $^5D_0 \rightarrow {}^7F_0$ transition of Eu^{3+} is prohibited according to the selection rule of magnetic dipole transition ($J = 0 \rightarrow J' = 0$). However, the presence of this transition indicates the violation of the Judd–Ofelt's selection rule, which may be ascribed to the asymmetry of the $[EuO_8]_{\text{deformed}}$ dodecahedron.[49] Herein, we believe that the asymmetry of the

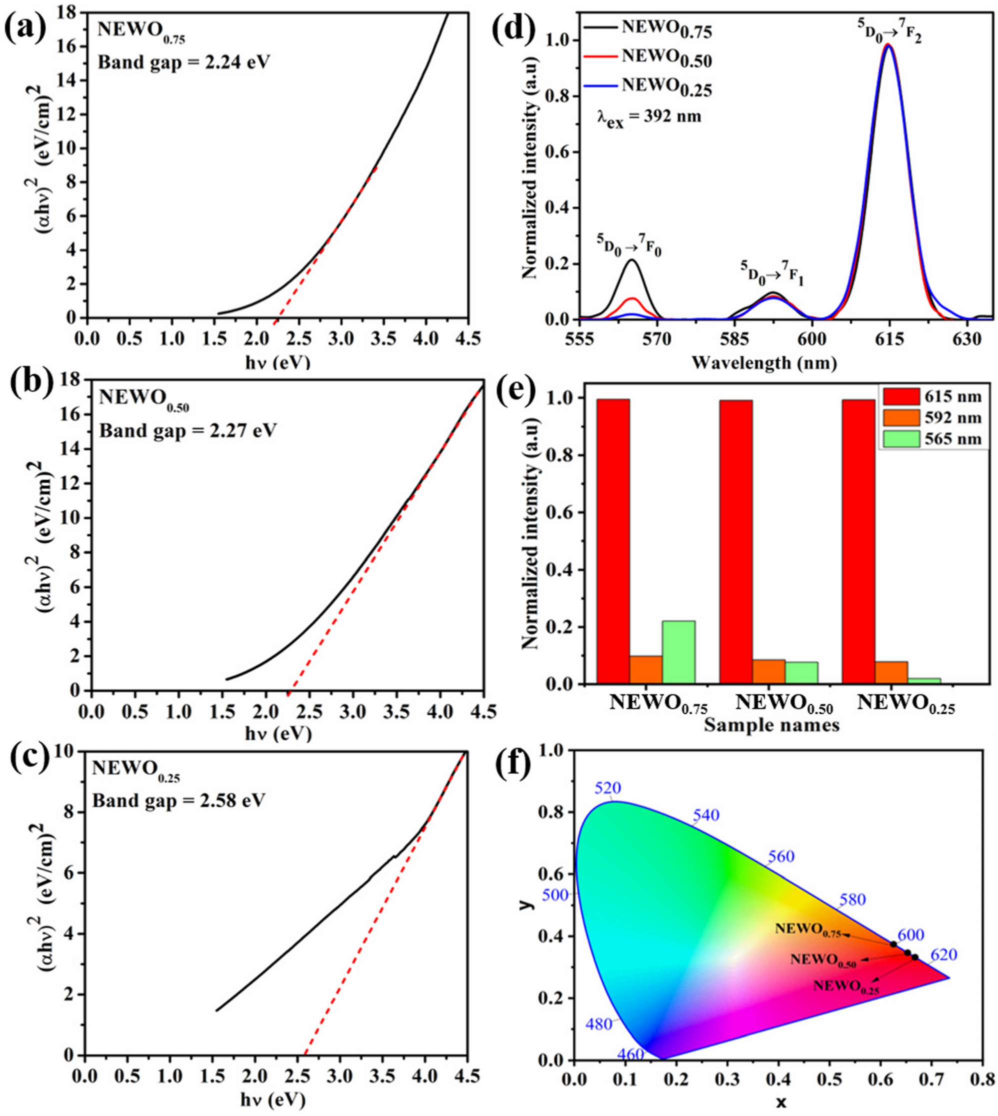

Fig. 5 Tauc plot: (a) $NEWO_{0.75}$, (b) $NEWO_{0.50}$, and (c) $NEWO_{0.25}$. (d) PL spectra of $NEWO_{0.75}$, $NEWO_{0.50}$, and $NEWO_{0.25}$. (e) Bar diagram of the normalized PL intensity of samples and (f) CIE diagram of $NEWO_{0.75}$, $NEWO_{0.50}$, and $NEWO_{0.25}$ samples.

crystal lattice leads to wavefunction mixing between the $^7F_0$ and $^7F_2$ states (discussed later). In this context, the second-order parameter (B_{20}) of the crystal field expansion plays a pivotal role in the mixing of the wavefunctions and is related to the intensity of $^5D_0 \rightarrow {}^7F_0$ and $^5D_0 \rightarrow {}^7F_2$ transitions by the following eqn (8).[50]

$$\frac{I(^5D_0 - {}^7F_0)}{I(^5D_0 - {}^7F_2)} = \frac{4{B_{20}}^2}{75{\varDelta_{20}}^2} \tag{8}$$

where $\varDelta_{20}$ (=1439 cm^{-1}) denotes the energy gap between the $^7F_0$ and $^7F_2$ levels. In this calculation, B_{20} was found to be 623, 1393 and 2492 cm^{-1} for $NEWO_{0.25}$, $NEWO_{0.50}$ and $NEWO_{0.75}$, respectively. These values of the B_{20} parameter are within the range of few other materials such as YPO4:Eu^{3+} (1365 cm^{-1}), $Ca(PO_3)_2$:Eu^{3+} (1600 cm^{-1}), and K–Al–B–Te:Eu^{3+} (829 cm^{-1}), which suggests the reliability of our estimated B_{20} parameters.[51] In this context, it may be stated that a smaller magnitude of the B_{20} parameter indicates a low degree of crystal field perturbation (denoted by the asymmetric $^5D_0 \rightarrow {}^7F_0$ transition at 565 nm, shown in the bar diagram in Fig. 5(e)); thus, the decreasing trend of B_{20} from $NEWO_{0.75}$ to $NEWO_{0.25}$ can be certainly attributed to the lowering of $[EuO_8]_{deformed}$ in our synthesized samples and corroborates highly with the Rietveld, FTIR and XPS studies. The quantum yield (QY), of $NEWO_{0.25}$, calculated from the photoluminescence decay profile (shown in Fig. S6(b), ESI†) using the relation $QY = \frac{\frac{1}{\tau_2}}{\frac{1}{\tau_1} + \frac{1}{\tau_2}}$ (where, τ_1 and τ_2 denote non-radiative and radiative recombination times), is ∼50%, which is slightly less than the QY of other scheelite materials.[52,53]

Furthermore, the colour feature, indicated by the color coordinate (x, y) in the Commission International de I'Eclariage (CIE) chromaticity diagram (shown in Fig. 5(f)), has been examined for our synthesized samples. As presented in

Table 2, the color coordinates of all the samples are observed within the red region, which may be attributed to the strong emission at 615 nm. Most importantly, $NEWO_{0.25}$ exhibits improved colour coordinate from the commercially available red $Y_2O_2S:Eu^{3+}$ phosphor (0.63, 0.35),[54] which perfectly matches with the standard color coordinate (0.67, 0.33) according to NTSC. Colour purity (CP) of ~86.7, 93.6 and 97.1% for $NEWO_{0.75}$, $NEWO_{0.50}$ and $NEWO_{0.25}$ was calculated using the following eqn (9)[38]

$$CP = \frac{\sqrt{(x - x_i)^2 + (y - y_i)^2}}{\sqrt{(x_d - x_i)^2 + (y_d - y_i)^2}} \times 100\% \tag{9}$$

where (x, y) is the CIE coordinate of the $NaEu(WO_4)_2$ samples, (x_i, y_i) is the illuminate point of the 1931 CIE Standard Source C with the colour coordinates of (0.3101, 0.3162), and (x_d, y_d) is the colour coordinate of the dominant wavelength. Herein, the correlated colour temperatures (CCTs) of ~1747, 2365 and 2957 K for $NEWO_{0.75}$, $NEWO_{0.50}$ and $NEWO_{0.25}$, respectively, were calculated using the McCamy relation eqn (10)[55]

$$CCT = 449n^3 + 3525n^2 + 6823.3n + 5520.3 \tag{10}$$

where $n = \frac{(x - 0.3320)}{(y - 0.1858)}$; (x, y) represent the chromaticity coordinate. These results suggest that $NaEu(WO_4)_2$ may be a potential candidate for red emission with excellent color purity and color coordinates close to the NTSC norms.

4. Investigation of the gas sensing properties of $NaEu(WO_4)_2$

The gas sensing property of any metal oxide mostly depends on the gas–solid interaction with target gas molecules, wherein the adsorption/desorption of the gas molecule leads to a significant change in the resistance of the material. Previous studies by several researchers including our group reveal that V_O traps electrons (e′), acts as a donor level within E_g and plays a pivotal role in both optical and gas sensing.[15,18,67–72] For metal oxide sensors, V_O facilitates receptor and transducer functions, which in turn tune the interaction of the target gas molecule on the sensor surface and transportation of the generated electronic signal within the sensor. It is an accepted mechanism that V_O enhances the chemisorption of atmospheric O_2, as described by $O_2(gas) + e^- \leftrightarrow O_2^-(ads)$[73] and facilitates the receptor activity by oxidizing more of the target gas molecules. Herein, a careful literature survey shows that $O_2^-(ads)$ can facilitate the following redox reactions between NEWO samples and acetone (CH_3COCH_3), ethanol (C_2H_5OH), ammonia (NH_3), methanol (CH_3OH), and formaldehyde (HCHO), as presented by eqn (11)–(15).

$$CH_3COCH_3(gas) + 8O_2^-(ads) \leftrightarrow 3H_2O(gas) + 3CO_2(gas) + 8e^- \tag{11}$$

$$CH_3CH_2OH(gas) + O_2^-(ads) \leftrightarrow 2H_2O(gas) + C_2H_2O + 2e^- \tag{12}$$

$$4NH_3(gas) + 3O_2^-(ads) \leftrightarrow 6H_2O(gas) + 2N_2(gas) + 3e^- \tag{13}$$

$$CH_3OH(gas) + O_2^-(ads) \leftrightarrow 2H_2O(gas) + CO(gas) + 2e^- \tag{14}$$

$$HCHO(gas) + O_2^-(ads) \leftrightarrow H_2O(gas) + CO_2(gas) + 2e^- \tag{15}$$

These electrons released at the defect state at the conduction band minima act as donors, thus improving the response significantly. As XPS analyses reveals the presence of $O_2(ads)$ formed within the $[EuO_8]_{deformed}$ dodecahedron, hence, the gas sensing property can be expected from NEWO samples. In order to validate the gas sensing ability of our synthesized NEWO samples as a proof-of-concept, we carried out a series of resistive-type sensing measurements using $NEWO_{0.75}$, $NEWO_{0.50}$ and $NEWO_{0.25}$ as sensor probes against NH_3, CH_3COCH_3, C_2H_5OH, CH_3OH, HCHO and IPA (C_3H_8O) at room temperature. As shown in Fig. 6(a), $NEWO_{0.75}$ exhibits highly selective sensitivity against CH_3COCH_3 in comparison with other target gases such as *etc.* as its resistance changes, while no significant variation was observed for other gases ($S = \left(\frac{R_{gas} - R_{air}}{R_{air}} \times 100\right)$, which was 5%, 3%, 8%, 4% and 6% for C_2H_5OH, NH_3, HCHO, CH_3OH and C_3H_8O, respectively). Room temperature operational condition is ascribed to the low bond-dissociation energy of CH_3COCH_3 (393 kJ mol^{-1}), in comparison with C_2H_5OH (458 kJ mol^{-1}), NH_3 (435 kJ mol^{-1}), and CH_3OH (439 kJ mol^{-1}), while the absence of sensing activity of $NEWO_{0.50}$ and $NEWO_{0.25}$ can be assigned to the low $[EuO_8]_{deformed}$ content and can be explained as follows. The electron-depleted layer (L_D), formed due to $O_2^-(ads)$, also plays a pivotal role in transducing the electronic signal in sensing response. Normally, L_D is prominent for the V_O-enriched sample, leading to superior sensing response.[71] Our XPS studies reveal the highest $V_O^{n\bullet}$ content of $NEWO_{0.75}$, indicating the most efficient signal transduction in comparison with $NEWO_{0.25}$ and $NEWO_{0.50}$. Therefore, the high $V_O^{n\bullet}$ content of $NEWO_{0.75}$ is believed to play a significant role in sensing CH_3COCH_3, one of the highly

Table 2 List of the CIE co-ordinates of this work, commercial red phosphors and few synthesised red phosphors

		CIE coordinate		
Materials name		x	y	Ref.
$NEWO_{0.25}$		0.667	0.333	This work
$NEWO_{0.50}$		0.653	0.347	This work
$NEWO_{0.75}$		0.625	0.374	This work
NTSC value		0.67	0.33	56
Commercial red phosphors	$Y_2O_2S:Eu^{3+}$	0.63	0.35	54
	$Y_2O_3:Eu^{3+}$	0.49	0.32	57
$Ba_2Gd_{0.1}Eu_{0.9}(BO_3)_2Cl$		0.581	0.355	57
$Ba_2Bi_{0.4}Eu_{0.6}V_3O_{11}$		0.65	0.35	58
$KGd_{0.7}Eu_{0.3}TiO_4$		0.65	0.34	59
$Sr_3Y_{0.94}(PO_4)_3:0.06\ Eu^{3+}$		0.64	0.33	56
$Sr_{1.7}Zn_{0.3}CeO_4:Eu^{3+}$		0.60	0.34	60
$Ca_2Ga_2GeO_7:0.07Eu^{3+},0.07Na^+$		0.64	0.359	61
$CdWO_4:0.5\%Eu^{3+}$		0.6465	0.347	62
$Ca_3(PO_4)_2:0.04Eu^{3+}$		0.5776	0.2840	63
$YBO_3:Eu^{3+}$		0.655	0.345	64
$NaCaBO_3:0.11Eu^{3+}$		0.608	0.387	65
$Sr_2SiO_4:Eu^{3+}$		0.6106	0.3517	66

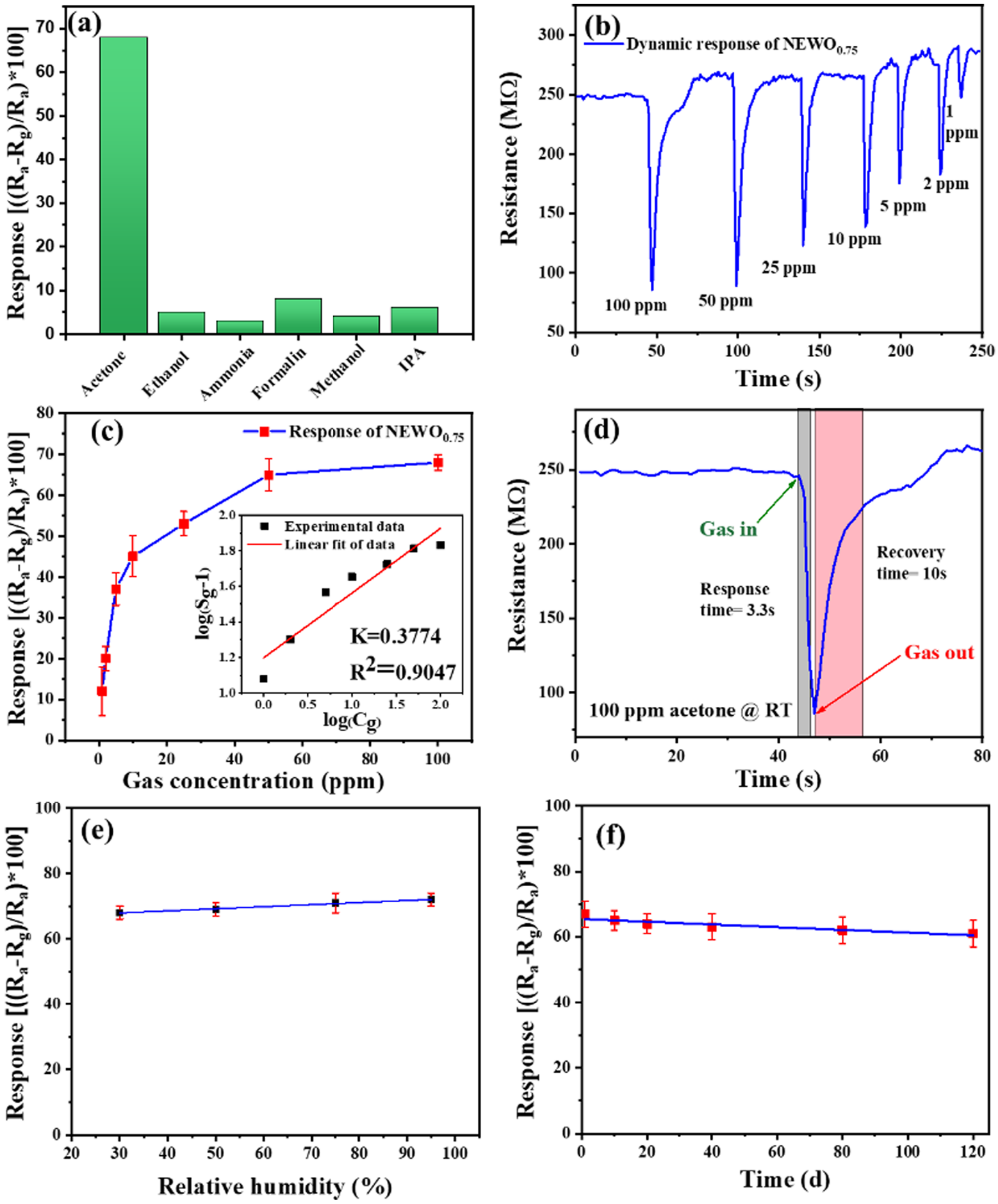

Fig. 6 (a) Selectivity of theNEWO$_{0.75}$ sensor toward acetone at RT. (b) Dynamic response curve of NEWO$_{0.75}$ when exposed to 1–100 ppm acetone at RT. (c) Acetone response value of NEWO$_{0.75}$ as a function of acetone concentration at RT (inset: isotherm fitting of the acetone response value of NEWO$_{0.75}$ with linear regression). (d) Response and recovery time of the NEWO$_{0.75}$ sensor for 100 ppm acetone at RT. (e) Response data at different %RH values to 100 ppm acetone at RT. (f) Long-term stability data of the NEWO$_{0.75}$ sensor to 100 ppm acetone for 120 days.

flammable VOCs that cause difficulties in breathing, nausea, vomiting and symptoms of neurological poisoning and also as a biomarker of diabetes found in exhaled human breath.[74,75]

Dynamic response, tested by exposing the sensor to different concentrations of CH_3COCH_3 ranging from 1 to 100 ppm (Fig. 6(b)), illustrates that the response increases gradually with increasing CH_3COCH_3 concentration, while Fig. 6(c) depicts the response of NEWO$_{0.75}$ as a function of CH_3COCH_3 concentration. Herein, it may be concluded from Fig. 6(c) that the NEWO$_{0.75}$ sensor has the capability to detect CH_3COCH_3 down to 1 ppm with changes in the resistance of ∼12% at room temperature, while the response increases to ∼68% at 100 ppm CH_3COCH_3 saturating above 100 ppm. To understand the adsorption/desorption mechanism, we fitted the response data with the Freundlich adsorption isotherm, as given by eqn (16) and (17).

$$S_g = 1 + aC_g^b \tag{16}$$

$$i.e.\ \log(S_g - 1) = a + b\log(C_g) \tag{17}$$

where, S_g and C_g are the sensitivity and concentration of the target gas, while "a" and "b" denote the constants that depend on the electrical charge of the surface species and stoichiometry of the surface reaction. As is known from previous reports, $b < 0.5$ indicates physisorption process, while $b > 1$ denotes chemisorption mechanism.[76] Currently, the linear characteristic between $\log(S_g - 1)$ and $\log(C_g)$, as shown in the inset of

Fig. 6(c), provides b = 0.38, indicating the physisorption of CH_3COCH_3 on the surface of $NEWO_{0.75}$. Response and recovery time of ∼3.3 s/10 s in the presence of 100 ppm CH_3COCH_3 indicate that the sensor is suitable for ultrafast application, as shown in Fig. 6(d). The repeatability, studied by exposing the sensor to seven consecutive cycles of exposure to 10 ppm acetone at room temperature (shown in Fig. S7, ESI†), gives almost similar characteristics (≤4% variation) for each measurement, yielding the excellent repeatability of $NEWO_{0.75}$ as a sensor material. The performance of the sensor was also checked under different humidity conditions, wherein our sensor shows highly robust performance under humidity (Fig. 6(e)). The long-term stability of the senor (presented in Fig. 6(f)), tested over 120 days, shows the negligible deterioration of the response. In this context, we compared the CH_3COCH_3 response characteristics in the previous literature and have presented a study in Table 3. It can be stated here that $NaEu(WO_4)_2$ exhibits the best response characteristics (∼68% to 100 ppm acetone) with very short response–recovery time, and most importantly, it works at room temperature, indicating the reliability of the $NaEu(WO_4)_2$-based sensor for different non-invasive applications.

Presently, the high selectivity of $NaEu(WO_4)_2$ towards CH_3COCH_3 sensing can be understood as the lowering of bond dissociation energy (BDE) in comparison with other VOCs. According to the previous reports,[87–90] the BDE of acetone is 393 kJ mol^{-1}, whereas that of other gases is as follows: ethanol, 458 kJ mol^{-1}; ammonia, 435 kJ mol^{-1}; methanol, 439 kJ mol^{-1}; formaldehyde, 364 kJ mol^{-1}; and IPA, 440 kJ mol^{-1}. During the adsorption of the gas molecules, acetone molecules will break more easily, allowing them to participate in the reaction process. However, the gas molecules having higher BDE would be less likely to react with the sensor material at low operating temperature (RT). It is interesting to note that even though the BDE of formaldehyde is in the range comparable to that of acetone, the sensor showed lower response to formaldehyde. This can be attributed to the electron donating effect during the reduction process of the target gases. As given in eqn (11)–(15), it is evident that during the reduction process of acetone, a greater number of electrons are released that contribute to the highest sensitivity and makes the sensor selective to acetone than any other target gas. Additionally, acetone molecules are known to have a large dipole moment (μ = 2.91 D).[91,92] Therefore, there will be a strong interaction between acetone and the sensing layer of $NEWO_{0.75}$, resulting in high response.

5. Computational analysis of ordered and disordered $NaEu(WO_4)_2$

To perceive a deep insight on the effect of the $Eu_{Na}^{m\bullet}$ antisite defect on optical and gas sensing properties, we carried out a series of *ab initio* calculations of electronic structure using density functional theory. Prior to examining the $Eu_{Na}^{m\bullet}$ antisite effects, we calculated the electronic structure along high symmetry points within the Brillouin zone, total density of states (TDOS), and angular momentum projected partial density of states (PDOS) of perfectly ordered NEWO ($NEWO_{order}$). In this calculation, we optimized the unit cell structure and obtained lattice parameters $a = b \sim 5.215$ Å and $c \sim 11.511$ Å, Eu–O bond lengths ∼2.461 and 2.460 Å, W–O ∼1.783 Å and $\Delta_{Eu-O} = 0.04$, which match closely with the experimentally measured parameters, indicating the good choice of the exchange potential for our calculations. In these calculations, the top of the valence band maxima (VBM) was set at zero. The electronic band structure (shown in Fig. 7(a)) of $NEWO_{order}$ exhibits $E_g \sim 3.29$ eV with both valence band maxima (VBM) and conduction band minima (CBM) at the Γ-point. TDOS and PDOS calculations (shown in Fig. 7(b)–(f)) demonstrate the predominant contribution of O $2p_x$, $2p_y$ and Eu 4f orbitals in following order $4f_{z^3} > 4f_{xz^2} > 4f_{zx^3} > 4f_{y^3x^2} > 4f_{yz^2}$, $4f_{x^3}$, $4f_{xyz}$ to the upper part of the valence band, while the lower part mostly consists of W $4d_{xz}$, $4d_{z^2}$, $4d_{xy}$ and O $2p_z$. The lower part of the conduction band mostly comprises the hybridization of W $4d_{z^2}$, $4d_{x^2}$ O $2p_z$ orbitals, whereas the upper part mostly consists of Eu 4f–O $2p_x$, $2p_y$ orbitals. As the electronegativity of Eu (1.2) is lower than that of W (2.36) on the empirical Pauling electronegativity scale, hence, Eu 4f orbitals should lie above the W 4d orbitals, which corroborates well with our calculations. Among different orbitals, the VBM and CBM of NEWO mostly originate from the hybridization of Eu $4f_{xyz}$–O $2p_x$, $2p_y$ and W $4d_{z^2}$–O $2p_z$, respectively. Therefore, it may be stated that the VB to CB electronic transition is associated with the charge transfer from the EuO_8 dodecahedron to the WO_4 tetrahedron. The band structure, TDOS and PDOS calculations of the disordered samples

Table 3 The sensing performance of various metal oxides toward acetone gas

Material name (type)	Operating temperature (°C)	Response/recovery time (s)	Acetone response value (in ppm)	Ref.
$NEWO_{0.75}$	Room temperature	3.3/10	68 (100 ppm)	This work
0.5% Fe–ZnO	365	3/12	105.7 (100 ppm)	77
Pt–Fe_2O_3	139	3/22	25.7 (100 ppm)	78
$ZnFe_2O_4$	220	23/9	64.9 (50 ppm)	79
SnO_2	370	9.7/5.8	50.2 (200 ppm)	80
WO_3	320	5/5	32 (100 ppm)	81
TiO_2	400	0.75/0.5	21.6 (200 ppm)	82
Co_3O_4	240	2/5	4.88 (500 ppm)	83
$PrFeO_3$	180	5/5	32.5 (50 ppm)	84
In_2O_3	300	0.7/14	29.8 (50 ppm)	85
$La_{0.7}Sr_{0.3}FeO_3$	275	20/270	0.7 (500 ppm)	86

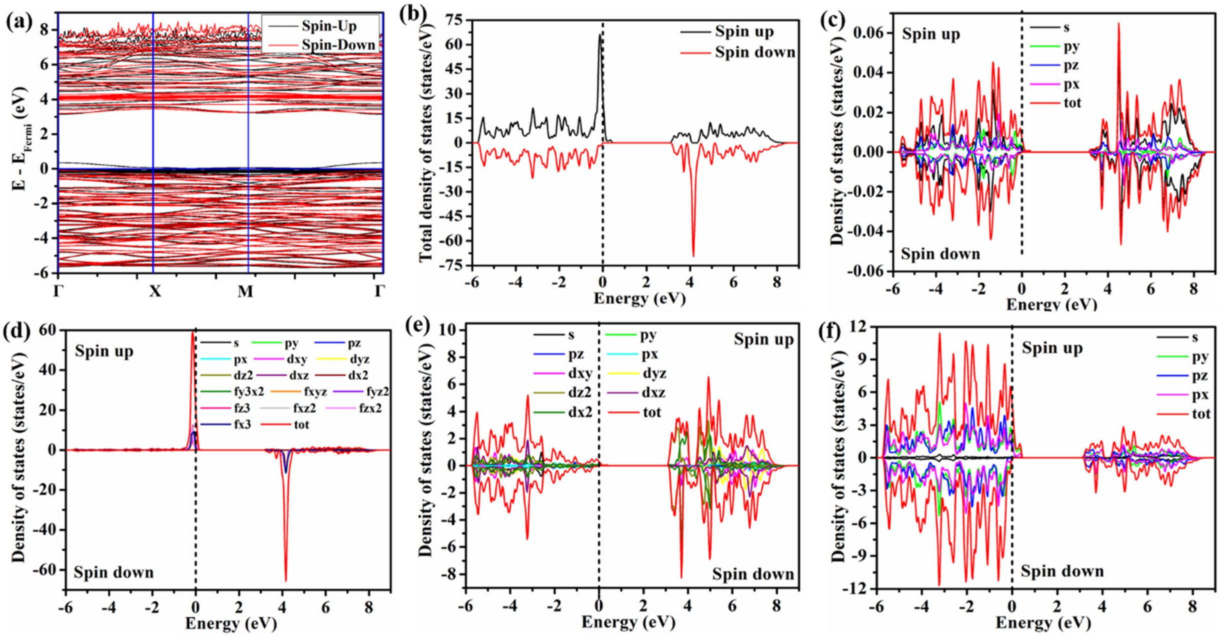

Fig. 7 DFT of $NEWO_{order}$: (a) band structure, (b) TDOS, (c) DOS of Na, (d) DOS of Eu, (e) DOS of W, and (f) DOS of O.

(shown in Fig. S8–S10, ESI†) give $E_g \sim 1.77$, 1.47 and 0.77 eV for $NEWO_{0.25}$, $NEWO_{0.50}$ and $NEWO_{0.75}$, respectively; thus, the decreasing trend of E_g agrees well with the experimental results. Though the VBM remains unchanged at *Γ*-point for all the samples, however, the CBM is shifted to the *M*-point for $NEWO_{0.50}$ and $NEWO_{0.75}$, indicating a change in the E_g from direct to indirect. PDOS and TDOS illustrate that all the orbitals get delocalized in the disordered samples with respect to $NEWO_{order}$, indicating enhanced bonding hybridization among the Eu 4f, O 2p and W 4d orbitals. Therefore, the observed phenomenon of enhanced second-order parameter (B_{20}) is certainly ascribed to the mixing of the orbitals $4f_{z^3}$, $4f_{xz^2}$, $4f_{y^3x^2}$, $4f_{yz^2}$, $4f_{x^3}$, $4f_{xyz}$ while, most importantly, the $4f_{zx^2}$ orbital does not contribute to this variation. However, significant modifications have been noted for the conduction band; more specifically, the delocalization and red shifting observed for W

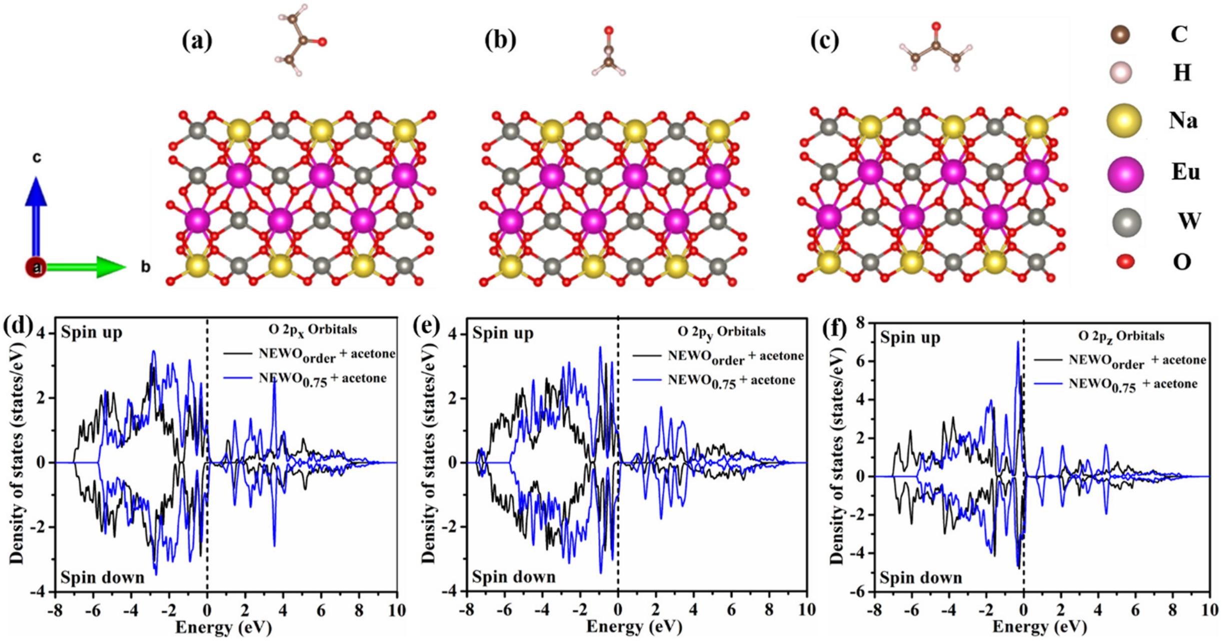

Fig. 8 Three possible layouts of the acetone molecule and the (0 0 4) plane surface of the $NEWO_{0.75}$ material: (a) vertical position, (b) parallel to *x*-axis and (c) parallel to *y*-axis position. PDOS plot of the (0 0 4) slab surface + acetone molecule: (d) O $2p_x$ orbitals, (e) O $2p_y$ orbitals, and (f) O $2p_z$ orbitals.

Table 4 Adsorption energy of acetone gas on the (0 0 4) plane surface of targeted nanomaterials

Target materials	Adsorption energy		
	Vertical position	Parallel *X* position	Parallel *Y* position
$NEWO_{order}$	−1.20	+0.45	+0.42
$NEWO_{0.75}$	−1.30	+0.19	+0.18

$4d_{z^2}$, $4d_{x^2}$ and O $2p_z$ orbitals are attributed to the increase in the W–O bond length; thus, the reduction of E_g is assigned to the red shifting of the W $4d_{z^2}$, $4d_{x^2}$ and O $2p_z$ states. The high density of states of Eu 4f in the conduction band, found in the deformed samples and assigned to the higher $Eu_{Na}^{m\bullet}$ antisite defect, agree well with the enhanced emission corresponding to the f–f transitions of Eu^{3+} ions.

Furthermore, in order to understand the effect of $Eu_{Na}^{m\bullet}$ antisite effects on the sensing performances, we examined CH_3COCH_3 adsorption on $NEWO_{order}$ and $NEWO_{0.75}$, while the calculation was performed using three different orientations of the CH_3COCH_3 molecule (shown in Fig. 8(a)–(c)) on the (0 0 4) plane as the model plane for adsorption. As depicted in Table 4, CH_3COCH_3 adsorption has been found to be stable in vertical configuration and most importantly, we notice the most negative CH_3COCH_3 adsorption energy for $NEWO_{0.75}$ in comparison with $NEWO_{order}$, indicating the greater stability of CH_3COCH_3 on the (0 0 4) plane of $NEWO_{0.75}$. We observed an optimized distance between the adsorbed CH_3COCH_3 and sample surface of ∼2.9–3.2 Å, which is larger than the sum of the corresponding atomic covalent radii; hence, it may be stated that no direct chemical is formed between CH_3COCH_3 and the sample. It is noted (shown in Fig. 8(d)–(f)) that CH_3COCH_3 adsorption gives rise to additional O $2p_x$, $2p_y$ and $2p_z$ orbitals as impurity levels in between the valence and conduction bands. In addition, we also observed that the PDOS calculations of Eu 4f and W 4d orbitals get red-shifted, indicating a significant change in the conductivity of NEWO in the presence of CH_3COCH_3 (shown in Fig. S11 and S12, ESI†). However, this modification is found to be more significant in $NEWO_{0.75}$, suggesting the higher sensing performance of $NEWO_{0.75}$ with respect to $NEWO_{order}$. Therefore, it may be concluded that the $Eu_{Na}^{m\bullet}$ antisite defect related $V_O^{n\bullet}$ plays the most important role in CH_3COCH_3 sensing by $NaEu(WO_4)_2$ at room temperature, while conductivity changes mostly involve Eu 4f orbitals.

6. Conclusion

In summary, the present study reports the synthesis and characterization of the $Eu_{Na}^{m\bullet}$ antisite defect containing $NaEu(WO_4)_2$ synthesized at various concentrations of Na_3cit. Herein, we have identified that the $Eu_{Na}^{m\bullet}$ antisite defects that can be controlled by Na_3cit concentration during hydrothermal reaction have a significant effect on the structural deformation of the EuO_8 dodecahedron, covalence of the tungstate host and polarization around the Eu^{3+} ions. Due to the variation of the polarized field around Eu^{3+} ions, a significant mixing of the Eu 4f orbitals, followed by the relaxation of the f–f transition rule, was observed and because of this relaxation, $NaEu(WO_4)_2$ exhibits strong luminescence at 615 nm with colour coordinate (0.667, 0.333) and color purity ∼97.1% under near-UV excitation (392 nm), indicating its potency as a red phosphor material in LEDs. We identified the presence of $V_O^{n\bullet}$s and associated $Eu_{Na}^{m\bullet}$ antisite defects, and they act as the active sites for O_2 adsorption, which in consequence facilitates the CH_3COCH_3 sensing property. Most importantly, we have found the sensing property at room temperature, which is very rare but has tremendous technological importance due to the low power consumption. Our *ab initio* calculations show a deep understanding of the electronic structure of $NaEu(WO_4)_2$, wherein the VBM and CBM originate from Eu–O and W–O hybridizations, respectively, indicating a charge transfer optical band. Finally, it may be concluded that the prepared materials could be multifunctional materials that can work as both red phosphor and room-temperature acetone gas sensor through the tuning of the antisite defect with the control of the Na_3cit concentration.

Data availability

The data supporting the findings of this work are available within the article and its ESI.† Raw data that support the findings of this work are available from the corresponding authors (C. K. G.) upon reasonable request.

Conflicts of interest

There is no conflicts to declare.

Acknowledgements

One of the authors (K. R. S.) thanks UGC, Govt. of India (NTA Ref. no.: 191620049221) for financial support during execution of this work. The authors would also like to extend their appreciation to the Researchers Supporting Project number (RSPD2024R956), King Saud University, Riyadh, Saudi Arabia.

References

1 M. Yin, Y. Liu, L. Mei, M. S. Molokeev, Z. Huang and M. Fang, *RSC Adv.*, 2015, **5**, 73077–73082.
2 M. Laguna, N. O. Nuñez, A. I. Becerro and M. Ocaña, *CrystEngComm*, 2017, **19**, 1590–1600.
3 K. G. Sharma and N. R. Singh, *New J. Chem.*, 2013, **37**, 2784–2791.
4 H. Zhu, C. Liang and W. Huang, *Phys. B*, 2020, **582**, 411999.
5 X. Yu, Y. Jiang, X. Li, Z. Song, X. Zhang, H. Liu, B. Zhao, T. Ye, L. Duan and J. Fan, *CrystEngComm*, 2022, **24**, 805–817.
6 Y. Ding, J. Liu, M. Zeng, X. Wang, J. Shi, W. Wang, Y. Miao and X. Yu, *Dalton Trans.*, 2018, **47**, 8697–8705.
7 V. Mahalingam and J. Thirumalai, *RSC Adv.*, 2016, **6**, 80390–80397.
8 R. Singh, A. King and B. B. Nayak, *Optik*, 2021, **247**, 167870.
9 Y. Yang, C. Chen and Q. Wang, *J. Alloys Compd.*, 2024, 175042.

10 V. Chauhan, P. Dixit, P. K. Pandey, S. Chaturvedi and P. C. Pandey, *Methods Appl. Fluoresc.*, 2023, **12**, 015002.

11 L. Kong, H. Sun, Y. Nie, Y. Yan, R. Wang, Q. Ding, S. Zhang, H. Yu and G. Luan, *Molecules*, 2023, **28**, 2681.

12 J. Huang, J. Xu, H. Luo, X. Yu and Y. Li, *Inorg. Chem.*, 2011, **50**, 11487–11492.

13 S. Neeraj, N. Kijima and A. K. Cheetham, *Chem. Phys. Lett.*, 2004, **387**, 2–6.

14 N. Haldar, T. Mondal, A. Dutta, D. Sarkar, U. K. Ghorai and C. K. Ghosh, *Appl. Phys. A*, 2023, **129**, 708.

15 N. Haldar, T. Mondal, T. Das, D. Sarkar, M. Pal and C. K. Ghosh, *CrystEngComm*, 2023, **25**, 3514–3527.

16 A. K. Munirathnappa, A. K, A. K. Sinha and N. G. Sundaram, *Cryst. Growth Des.*, 2018, **18**, 253–263.

17 A. K. Munirathnappa, V. C. Petwal, J. Dwivedi and N. G. Sundaram, *New J. Chem.*, 2018, **42**, 2726–2732.

18 N. Haldar, T. Mondal, T. Das, D. Sarkar, M. Pal, A. H. Seikh and C. K. Ghosh, *Mater. Adv.*, 2024, **5**, 4480–4490.

19 S. Brahma, Y. W. Yeh, J. L. Huang and C. P. Liu, *Appl. Surf. Sci.*, 2021, **564**, 150351.

20 C. Li, H. Zhou, S. Yang, L. Wei, Z. Han, Y. Zhang and H. Pan, *ACS Appl. Nano Mater.*, 2019, **2**, 6144–6151.

21 F. A. Rabuffetti, S. P. Culver, L. Suescun and R. L. Brutchey, *Inorg. Chem.*, 2014, **53**, 1056–1061.

22 L. Li, Y. Su and G. Li, *Appl. Phys. Lett.*, 2007, **90**, 054105.

23 G. M. Kuz'Micheva, I. A. Kaurova, V. B. Rybakov, P. A. Eistrikh-Geller, E. V. Zharikov, D. A. Lis and K. A. Subbotin, *CrystEngComm*, 2016, **18**, 2921–2928.

24 Z. Xu, C. Li, G. Li, R. Chai, C. Peng, D. Yang and J. Lin, *J. Phys. Chem. C*, 2010, **114**, 2573–2582.

25 Y. Chen, S. W. Park, B. K. Moon, B. C. Choi, J. H. Jeong and C. Guo, *CrystEngComm*, 2013, **15**, 8255–8261.

26 S. Suwanboon, W. Somraksa, P. Amornpitoksuk and C. Randorn, *J. Alloys Compd.*, 2020, **832**, 154963.

27 J. Guo, D. Zhou, Y. Li, T. Shao, Z. M. Qi, B. B. Jin and H. Wang, *Dalton Trans.*, 2014, **43**, 11888–11896.

28 R. F. Gonçalves, L. S. Cavalcante, I. C. Nogueira, E. Longo, M. J. Godinho, J. C. Sczancoski, V. R. Mastelaro, I. M. Pinatti, I. L. V. Rosa and A. P. A. Marques, *CrystEngComm*, 2015, **17**, 1654–1666.

29 V. V. Popov, Y. V. Zubavichus, A. P. Menushenkov, A. A. Yastrebtsev, B. R. Gaynanov, S. G. Rudakov, A. A. Ivanov, F. E. Dubyago, R. D. Svetogorov, E. V. Khramov and N. A. Tsarenko, *Crystals*, 2022, **12**, 892.

30 Z. Mo, Z. Deng, R. Guo, Q. Fu, C. Feng, P. Liu and Y. Sun, *Mater. Sci. Eng., B*, 2012, **177**, 121–126.

31 H. Yang, D. Zhang, L. Shi and J. Fang, *Acta Mater.*, 2008, **56**, 955–967.

32 R. Gutkowski, C. Khare, F. Conzuelo, Y. U. Kayran, A. Ludwig and W. Schuhmann, *Energy Environ. Sci.*, 2017, **10**, 1213–1221.

33 J. V. B. Moura, C. Luz-Lima, G. S. Pinheiro and P. T. C. Freire, *Spectrochim. Acta, Part A*, 2019, **208**, 229–235.

34 L. S. Cavalcante, J. C. Sczancoski, J. W. M. Espinosa, J. A. Varela, P. S. Pizani and E. Longo, *J. Alloys Compd.*, 2009, **474**, 195–200.

35 N. Dirany, E. McRae and M. Arab, *CrystEngComm*, 2017, **19**, 5008–5021.

36 S. S. Bhat, D. Swain, C. Narayana, M. Feygenson, J. C. Neuefeind and N. G. Sundaram, *Cryst. Growth Des.*, 2014, **14**, 835–843.

37 A. K. Munirathnappa, D. Dwibedi, J. Hester, P. Barpanda, D. Swain, C. Narayana and N. G. Sundaram, *J. Phys. Chem. C*, 2018, **123**, 1041–1049.

38 B. P. Singh, J. Singh and R. A. Singh, *RSC Adv.*, 2014, **4**, 32605–32621.

39 H. Sun, B. Zhang, Q. Zhao, Y. Liu, R. Wu, S. Zhang, Y. Li and A. Chang, *J. Am. Ceram. Soc.*, 2022, **105**, 3715–3724.

40 P. W. Atkins, T. L. Overton, J. P. Rourke, M. T. Weller and F. A. Armstrong, *Inorg. Chem*, Oxford University Press, New York, 5th edn, 2010, p. 16.

41 S. K. Gupta, M. Sahu, P. S. Ghosh, D. Tyagi, M. K. Saxena and R. M. Kadam, *Dalton Trans.*, 2015, **44**, 18957–18969.

42 X. Wang, Z. Zhao, Q. Wu, C. Wang, Q. Wang, L. Yanyan and Y. Wang, *J. Mater. Chem. C*, 2016, **4**, 8795–8801.

43 P. Jena, S. K. Gupta, N. K. Verma, A. K. Singh and R. M. Kadam, *New J. Chem.*, 2017, **41**, 8947–8958.

44 B. Xu, X. Cao, G. Wang, Y. Li, Y. Wang and J. Su, *Dalton Trans.*, 2014, **43**, 11493–11501.

45 B. P. Singh, P. V. Ramakrishna, S. Singh, V. K. Sonu, S. Singh, P. Singh, A. Bahadur, R. A. Singh and S. B. Rai, *RSC Adv.*, 2015, **5**, 55977–55985.

46 X. Dong, Z. Fu, Y. Yu, S. Li and Z. Dai, *Mater. Lett.*, 2012, **74**, 140–142.

47 G. Rui, Q. Dong and L. Wei, *Trans. Nonferrous Met. Soc. China*, 2010, **20**, 432–436.

48 L. S. Zhao, J. Liu, Z. C. Wu and S. P. Kuang, *Spectrochim. Acta, Part A*, 2012, **87**, 228–231.

49 Z. Wang, J. Zhong, H. Jiang, J. Wang and H. Liang, *Cryst. Growth Des.*, 2014, **14**, 3767–3773.

50 A. K. Parchur and R. S. Ningthoujam, *RSC Adv.*, 2012, **2**, 10859–10868.

51 G. Nishimura and T. Kushida, *Phys. Rev. B: Condens. Matter Mater. Phys.*, 1988, **37**, 9075.

52 S. K. Gupta, P. S. Ghosh, M. Sahu, K. Bhattacharyya, R. Tewari and V. Natarajan, *RSC Adv.*, 2015, **5**, 58832–58842.

53 V. Mahalingam and J. Thirumalai, *J. Mater. Sci.: Mater. Electron.*, 2016, **27**, 8884–8890.

54 L. Jinglei, Y. U. Yan, L. Lingjie, S. Cheng, L. I. Guanyu and L. I. Nianbing, *J. Rare Earths*, 2012, **30**, 330–334.

55 M. Rai, G. Kaur, S. K. Singh and S. B. Rai, *Dalton Trans.*, 2015, **44**, 6184–6192.

56 B. Yang, Z. Yang, Y. Liu, F. Lu, P. Li, Y. Yang and X. Li, *Ceram. Int.*, 2012, **38**, 4895–4900.

57 H. Jing, C. Guo, N. Zhang, Z. Ren and J. Bai, *ECS J. Solid State Sci. Technol.*, 2012, **2**, R1.

58 J. Zhao, C. Guo, T. Li, X. Su, N. Zhang and J. Chen, *Dyes Pigm.*, 2016, **132**, 159–166.

59 N. Zhang, C. Guo, J. Zheng, X. Su and J. Zhao, *J. Mater. Chem. C*, 2014, **2**, 3988–3994.

60 H. Li, R. Zhao, Y. Jia, W. Sun, J. Fu, L. Jiang, S. Zhang, R. Pang and C. Li, *ACS Appl. Mater. Interfaces*, 2014, **6**, 3163–3169.

61 Y. Li, N. Li, P. Zhang, Z. Wei, Z. Wang, L. Zhao and W. Chen, *Spectrochim. Acta, Part A*, 2021, **248**, 119247.

62 M. You, J. Xu, Z. Zhang and Y. Zhou, *Ceram. Int.*, 2014, **40**, 16189–16194.

63 X. Zhang, L. Zhou and M. Gong, *Opt. Mater.*, 2013, **35**, 993–997.

64 R. S. Yadav, R. K. Dutta, M. Kumar and A. C. Pandey, *J. Lumin.*, 2009, **129**, 1078–1082.

65 X. Zhang, Y. Chen, S. Zeng, L. Zhou, J. Shi and M. Gong, *Ceram. Int.*, 2014, **40**, 14537–14541.

66 H. Liu, Y. Hao, H. Wang, J. Zhao, P. Huang and B. Xu, *J. Lumin.*, 2011, **131**, 2422–2426.

67 H. Ullah, Z. H. Yamani, A. Qurashi, J. Iqbal and K. Safeen, *J. Mater. Sci.: Mater. Electron.*, 2020, **31**, 17474–17481.

68 P. P. Ortega, B. Hangai, H. Moreno, L. S. R. Rocha, M. A. Ramírez, M. A. Ponce, E. Longo and A. Z. Simões, *J. Alloys Compd.*, 2021, **888**, 161517.

69 B. Sanches de Lima, P. R. Martinez-Alanis, F. Guell, W. A. dos Santos Silva, M. I. Bernardi, N. L. Marana, E. Longo, J. R. Sambrano and V. R. Mastelaro, *ACS Appl. Electron. Mater.*, 2021, **3**, 1447–1457.

70 Q. Zhang, G. Xie, M. Duan, Y. Liu, Y. Cai, M. Xu, K. Zhao, H. Tai, Y. Jiang and Y. Su, *ACS Appl. Nano Mater.*, 2023, **6**, 17445–17456.

71 R. T. Parayil, B. Bhagat, S. K. Gupta, K. Mukherjee and M. Mohapatra, *Phys. Chem. Chem. Phys.*, 2024, **26**, 7424–7434.

72 R. T. Parayil, S. K. Gupta, R. Rohilla, J. Prakash, K. Sudarshan and M. Mohapatra, *ACS Appl. Electron. Mater.*, 2023, **5**, 5151–5163.

73 T. Das, S. Mojumder, S. Chakraborty, D. Saha and M. Pal, *Appl. Surf. Sci.*, 2022, **602**, 154340.

74 J. Wu, Z. Zheng, H. Chi, J. Jiang, L. Zhu and Z. Ye, *ACS Appl. Mater. Interfaces*, 2024, **16**, 9126–9136.

75 K. Yuan, C. Y. Wang, L. Y. Zhu, Q. Cao, J. H. Yang, X. X. Li, W. Huang, Y. Y. Wang, H. L. Lu and D. W. Zhang, *ACS Appl. Mater. Interfaces*, 2020, **12**, 14095–14104.

76 T. Das, S. Mojumder, D. Saha and M. Pal, *Sens. Actuators, B*, 2024, **406**, 135358.

77 Y. Chen, H. Li, D. Huang, X. Wang, Y. Wang, W. Wang, M. Yi, Q. Cheng, Y. Song and G. Han, *Mater. Sci. Semicond. Process.*, 2022, **148**, 106807.

78 S. Zhang, M. Yang, K. Liang, A. Turak, B. Zhang, D. Meng, C. Wang, F. Qu, W. Cheng and M. Yang, *Sens. Actuators, B*, 2019, **290**, 59–67.

79 Z. Wen, H. Ren, D. Li, X. Lu, S. W. Joo and J. Huang, *Sens. Actuators, B*, 2023, **379**, 133287.

80 D. Chen, J. Xu, Z. Xie and G. Shen, *ACS Appl. Mater. Interfaces*, 2011, **3**, 2112–2117.

81 J. Lu, C. Xu, L. Cheng, N. Jia, J. Huang and C. Li, *Mater. Sci. Semicond. Process.*, 2019, **101**, 214–222.

82 W. Ge, S. Jiao, Z. Chang, X. He and Y. Li, *ACS Appl. Mater. Interfaces*, 2020, **12**, 13200–13207.

83 T. Zhou, T. Zhang, J. Deng, R. Zhang, Z. Lou and L. Wang, *Sens. Actuators, B*, 2017, **242**, 369–377.

84 L. Ma, S. Y. Ma, X. F. Shen, T. T. Wang, X. H. Jiang, Q. Chen, Z. Qiang, H. M. Yang and H. Chen, *Sens. Actuators, B*, 2018, **255**, 2546–2554.

85 X. Sun, H. Ji, X. Li, S. Cai and C. Zheng, *Mater. Lett.*, 2014, **120**, 287–291.

86 P. A. Murade, V. S. Sangawar, G. N. Chaudhari, V. D. Kapse and A. U. Bajpeyee, *Curr. Appl. Phys.*, 2011, **11**, 451–456.

87 H. Avireddy, H. Kannan, P. Shankar, G. K. Mani, A. J. Kulandaisamy and J. B. B. Rayappan, *Mater. Chem. Phys.*, 2018, **212**, 394–402.

88 H. Y. Lee, J. H. Bang, S. M. Majhi, A. Mirzaei, K. Y. Shin, D. J. Yu, W. Oum, S. Kang, M. L. Lee, S. S. Kim and H. W. Kim, *Sens. Actuators, B*, 2022, **359**, 131550.

89 S. Zhang, P. Song, J. Zhang, H. Yan, J. Li, Z. Yang and Q. Wang, *Sens. Actuators, B*, 2017, **242**, 983–993.

90 G. Feng, Y. Che, S. Wang, S. Wang, J. Hu, J. Xiao, C. Song and L. Jiang, *Sens. Actuators, B*, 2022, **367**, 132087.

91 C. N. Wang, M. X. Peng, L. J. Yue, X. Y. Yang and Y. H. Zhang, *Sens. Actuators, A*, 2022, **342**, 113650.

92 S. Neogi and R. Ghosh, *Sens. Actuators, B*, 2024, **415**, 135980.